Università degli Studi di Ferrara

DOTTORATO DI RICERCA IN

FISICA

CICLO XXXI

COORDINATRICE Prof.ssa Eleonora Luppi

DEVELOPMENT OF A GAMMA BEAM PROFILE IMAGER FOR ELI-NP-GBS

Dottoranda

Consoli Elisabetta

Tutore

Prof. Gambaccini Mauro

Anni 2015/2018

CONTENTS

INTRODUCTION

The work presented in this thesis was developed in the framework of the ELI (Extreme Light Infrastructure) project, a European initiative to create research facilities distributed over some of the latest EU member states of Central and Eastern Europe.

The ELI-Nuclear Physics (ELI-NP) facility, to be hosted near Bucharest (Romania), is the pillar of the ELI project dedicated to laser-matter interaction and nuclear physics studies.

This research infracstructure will host two machines of extreme performances: the High Power Laser System (HPLS), where beams from two 10 PW lasers are coherently added to obtain intensities up to 10^{23}–10^{24} W/cm^2), and the Gamma Beam Sysytem (GBS), the most brilliant tunable gamma-ray beam machine currently available in the world.

The ELI-NP gamma beam will be obtained by collimating the radiation emerging from inverse Compton scattering of short laser pulses on relativistic electron beam bunches produced by a warm linac. Using this method it will be possible to obtain a gamma beam with unprecedented characteristics such as tunable average energy ranging from 0.2 to 19.5 MeV, energy bandwidth down to 0.5% and flux of about 10^8 photons/s.

The GBS will consist of two parallel beamlines with two separated interaction points (IP): a low-energy line (LE) delivering gamma rays with energies up to 3.5 MeV and a high-energy line (HE) where the energy of the gamma rays will reach 19.5 MeV.

The provider of the GBS is the EuroGammas Consortium, a European association of academic, research institutions and industrial partners from all over Europe, led by I.N.F.N.

The role of I.N.F.N.-Ferrara has been the coordination of Work Package 09 (WP09) of EuroGammaS project, responsible for the design and realization of the characterization and collimation systems of the gamma beam. These activities have been carried out in collaboration with I.N.F.N. sections of Firenze and Catania.

The Gamma Beam Characterization system (GBC), essential to measure and monitor the beam parameters during the commissioning and the operational phase, consists of 4 different subsystems each carrying out different tasks: a Compton spectrometer (CSPEC), to measure and monitor the photon energy spectrum; a nuclear resonant scattering spectrometer (NRSS), for absolute beam energy calibration and inter-calibration of the other detectors; a sampling calorimeter (GCAL), for a fast combined measurement of the beam average energy and intensity, and a Gamma Profile Imager (GPI), to measure the spatial distribution and uniformity of the beam and to check the correct alignment of the collimation system with the source of the gamma beam emission.
The work presented in this dissertation concerns the design study, assembly and testing of the GPI.
This device is composed of a scintillator screen placed at 45 degrees with respect to the gamma beam direction, a CCD camera and a lens system to focus onto the CCD camera the scintillation light created by the interaction between the incident gamma-rays and the scintillator.
First activities were devoted to the characterization tests of the inorganic scintillating material selected as potential target for the GPI. Successively tests on the lens+camera system were performed in order to select the proper optical system configuration. Finally, a GPI prototype was assembled and tested by use of an X-ray tube in order to validate the analytical model and the simulation code adopted to predict the GPI performances.

The thesis is organized in four chapters. In the first the ELI-NP project is introduced and its main objectives in the physics research field are discussed. The Gamma Beam System is also described along with the collimation and characterization systems. The second chapter contains a review of the photon-matter interaction theoretical background as well as the inverse Compton scattering and the main characteristics of scintillator materials.

A description of the CCD working principle and thin lenses characteristics is also given.
In the third chapter the design study of the GPI is discussed and the final configuration adopted is described.
The fourth chapter gives a detail description of the experimental tests performed on the assembled GPI prototype. The results in terms of expected signal, evaluated by use of Monte Carlo simulations performed with Geant4, are also reported.

CHAPTER 1

THE ELI-NP FACILITY

1.1 – ELI: A European pioneristic project

The Extreme Light Infrastructure (ELI) project, [1],[2], is part of a European plan to build a new generation of large research facilities located in the new EU Member States.
ELI is designed as a laser facility and will use a new generation of laser technologies to create the most intense light pulses in the world, offering to the users new interdisciplinary research opportunities.
ELI is currently implemented as an infrastructure distributed in three pillars:

- ELI-Nuclear Physics (Magurele, Romania): aimed at exploring the scientific advanced potentials of a high intensity laser system (up to 10^{24} W/cm^2) joined with a high brilliance Gamma ray Beam System, in the field of Nuclear Physics and Nuclear Photonics.
- ELI-Beamlines (Prague, Czech Republic): devoted to the development and usage of dedicated beam lines with ultra short pulses of high energy radiation and particles reaching almost the speed of light.
- ELI-Attosecond (Szeged, Hungary): designed to conduct temporal investigation of electron dynamics in atoms, molecules, plasmas and solids at attosecond scale (10^{-18} s).

A fourth pillar of Ultra High Field Science (UHFS) targeting unprecedented laser field strength is further considered for the future, the location of which is to be decided.

The ELI project, approved by the Council of European Union, belongs to the ESFRI roadmap published in 2006, which is the list of the main research infrastructure of pan-european interest with a complete development foreseen within the next ten years [3]. From a technical point of view, the most important scientific result expected is the extension of the laser-matter interaction field from relativistic to the ultra-relativistic regime, which in terms of laser intensities means an increment of six orders of magnitude from 10^{20} W/cm^2 to 10^{26} W/cm^2. Also a compression of the duration of laser pulses will be achieved, from femtosecond to attosecond or zeptosecond (10^{-21} seconds) regime.
The mentioned improvement in laser field will open the possibility to study electron dynamics in atoms, molecules, plasmas and solids up to the zeptosecond time scale.
Another important objective will be the possibility to create ultra-short energetic particle (from 10 to 100 GeV) and radiation (up to a few MeV) beams produced for various applications.
ELI wants to provide the world-wide scientific community with a very important and historical boost in laser field research, and besides it guarantees a fundamental benefit for industry and society, holding new prospects in engineering and medical field.

1.2 – ELI-NP Nuclear Physics

ELI-NP, as already introduced, is one of the main facilities of the ELI project and it is located in Magurele, a town a few kilometers away from Bucharest, Romania [4].
ELI-NP will comprise two machines of extreme performances:
- High Power Laser System (HPLS), a very high intensity laser, obtained by coherently adding two 10 PW laser to reach an intensity of the order of 10^{23}-10^{24} W/cm^2 and electrical fields of 10^{15} V/m;
- Gamma Beam System (GBS), a very intense and brilliant gamma beam obtained by inverse Compton scattering of a laser light scattered by an accelerated electron beam produced by a warm LINAC.

The single or combined application of the two machines, as published in the ELI-NP White Book [5], an official document elaborated by more than 100 scienists taking part to the project from 30 countries, is expected to allow a wide range of experiments in the fields of nuclear physics, astrophysics and high energy physics.
In particular major progress will be achieved in nuclear physics and its associated fields:

- Investigation of a high power laser interaction with matter using nuclear physics methods in order to study the possibilities of obtaining high quality proton and heavy ion accelerated beams.
- The extremely high intensity of the laser beam will allow the study of fundamental physics phenomena anticipated by theory, such as vacuum birefringerance and pair creation in intense electric fields.
- Investigation of nuclear structure and cross sections of interest for astophysics using photonuclear reactions.
- New and more efficient methods for the production of radioisotopes currently used in medicine and newly proposed.

1.3 - ELI-NP Gamma Beam System

In this section a detailed description of the Gamma beam System is given.

1.3.1 The Gamma Beam System

The Gamma Beam System of ELI-NP, as already mentioned, is an advanced source of gamma-ray photons. It will be obtained by collimating the photons emerging from the inverse Compton interaction of optical photons with an electron beam previously accelerated by a warm LINAC up to 720 MeV.
This method will allow the production of very brilliant, highly mono-chromatic gamma rays with energies tunable up to almost 20

MeV. The properties of the gamma-ray beam provided by the system are listed in table 1.1 [6].

Parameter	Value
Photon energy	0.2–19.5 MeV
Bandwidth	≤0.5%
Spectral density	$(0.8–4)10^4$ ph/s/eV
# photons per pulse within FWHM bdw.	$\leq 2.6 \times 10^5$
Number of pulses/macro-pulse	32
Source rms size	10–30 μm
Source rms divergence	25–200 μrad
Peak brilliance	10^{20}–10^{23} $(\frac{1}{\text{sec}\cdot\text{mm}^2\text{mrad}^2 0.1\%\text{BW}})$
Linear polarization	>99%
Energy jitter pulse-to-pulse	<0.2%
# photons jitter pulse-to-pulse	≤ 3 %
Macro repetition rate	100 Hz
Pulse-to-pulse separation	16 ns

Table 1.1 - GBS beam output specifications [6].

The availability of γ-ray beams with such unprecedented features will make it possible to design and perform new classes of nuclear photonics and nuclear physics advanced experiments which cannot be done elsewhere.
For example, the γ-ray beam brilliance and bandwidth at ELI-NP will increase the sensitivity of nuclear resonance fluorescence (NRF) experiments prompting the opportunity to perform unique NRF studies on small target samples. This opens up an entire new area of applicability of the NRF method to materials that may be available only in quantities of a few milligrams.

ELI-NP-GBS is hosted and managed by the Horia Hulubei National Institute for Physics and Nuclear Engineering (IFIN-HH) of Magurele [7]. In order to achieve the desired specifications described above, in 2014 the IFIN-HH made an international call for tender to design, realise and commission the GBS. The tender was won by a European consortium called EuroGammaS.

Next section is dedicated to the description of EuroGammaS proposal for ELI-NP-GBS.

1.3.2 Eurogammas Consortium

EuroGammaS is a European consortium born in 2012 to prepare a proposal for the realization of the Gamma Beam System [8]. The realization includes design, manufacturing, delivery, installation, testing, commissioning and maintenance of the apparatus. The collaboration involves Università degli Studi di Roma La Sapienza, Centre National de la Recherche Scientifique, ACP S.A.S., Alsyom S.A.S., Comeb Srl, ScandiNova Systems AB and the Istituto Nazionale di Fisica Nucleare INFN, which is the association leader. Within the collaboration, the role of INFN-Ferrara research team consists in the coordination of Work Package 09 (WP09) of EuroGammaS project, that concern the characterization and collimation of the gamma beam. These activities are done in collaboration with INFN sections of Firenze and Catania. In the following paragraphs a summary of the characteristics of the GBS design proposed by EuroGammas collaboration will be given, briefly describing the apparatus involved in the gamma beam production, collimation and characterization.
In figure 1.1 an overview of the GBS is depicted.

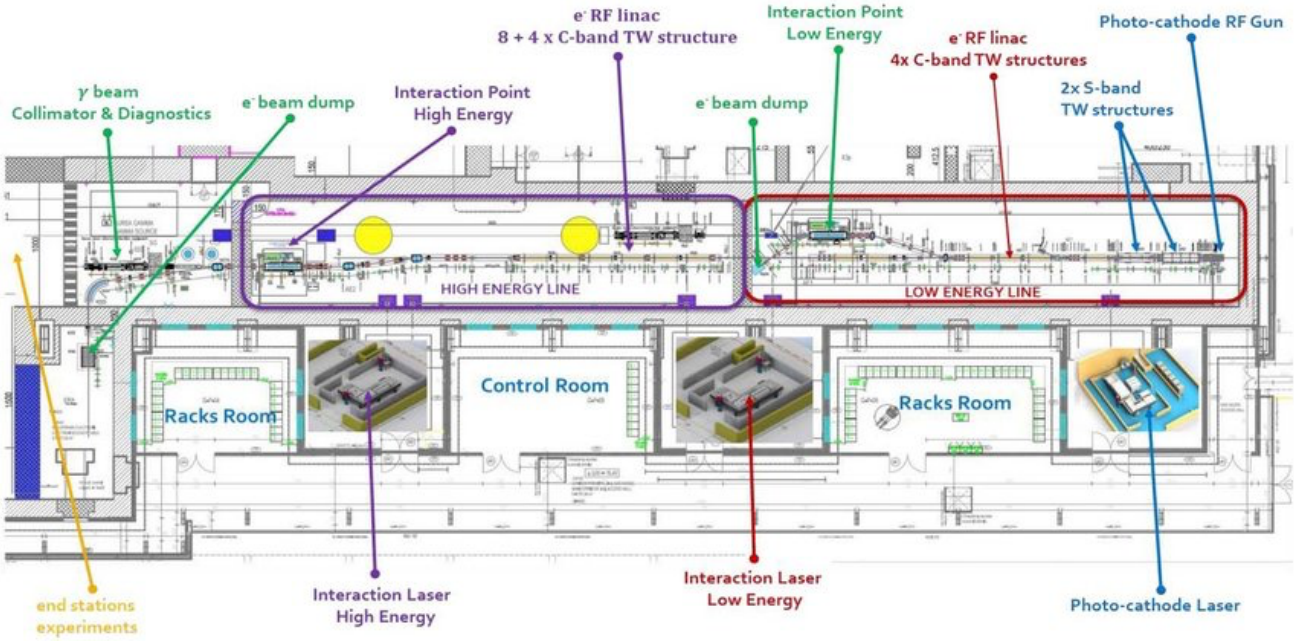

Figure 1.1 - Layout of the Gamma Beam System

1.3.3 GBS production and collimation

Conceptually, the Gamma Beam System is composed of a laser providing photon pulses that are up-shifted in energy to MeV range or above through collision with relativistic electron bunches produced by a linear accelerator. The resulting incoherent gamma rays form a low divergence microbeam that can be well defined in energy by adequate collimation.

A description of the main components involved in the production of the Gamma Beam System is given below.

Electron accelerator and laser system: the electron accelerator is a high brightness normal conducting LINAC consisting of two S-band and twelve C- band RF structures.

The LINAC is designed to work in two phases: in the first electrons are accelerated up to 360 MeV, in the second up to 720 MeV, in these two phases a low energy and a high energy gamma beam are created respectively. In particular, in the first line the gamma beam achievable energy ranges from 0,2 to 3,5 MeV, in the

second from 3,5 to 19,5 MeV. In figure 1.1 it is possible to observe the position of the interaction points between electrons and optical photons. At the end of Linac 1 electrons may be deviated from their acceleration trajectory in order to undergo the interaction for the production of the low energy gamma beam; otherwise, electrons continue to be accelerated and interact with the optical laser at the end of Linac 2, where the high energy gamma beam may be extracted.

The accelerator is designed to work with Radio-Frequencies (RF) fixed on a value equal to 100 Hz. For each RF pulse, a packet made of 32 microbunches of accelerated electrons, separated by a time interval equal to 16 ns, is produced. In order to cope with the low cross section of the process, each laser pulse will undergo a recirculation system, schematically represented in figure 1.2, that permits to reiterate the interaction of the same pulse 32 times (16 + 16 with slightly divergent angles of incidence) with the same number of different electron bunches. In this way it is possible to increase the yield rate of the gamma rays production. The time separation between each recirculation is 16 ns and the electron bunches will be synchronized with this time pattern. This will result in the temporal structure of the gamma beam represented in figure 1.3: it will be composed by macro-pulses with a time separation of 10 ms (100 Hz); each macro-pulse is made of 32 pulses characterized by a duration of about 1,5 ps and separated by a 16 ns time interval [9],[10],[11].

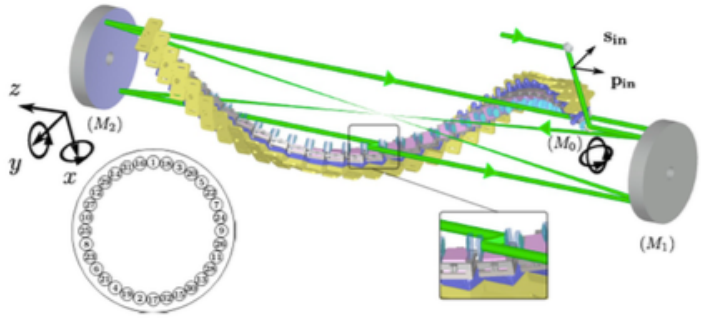

Figure 1.2 - Schematic rapresentation of the Recirculation System adopted at GBS. This particular layout of mirrors is able to focus the same laser pulse and force it passing 32 times through the interaction point.

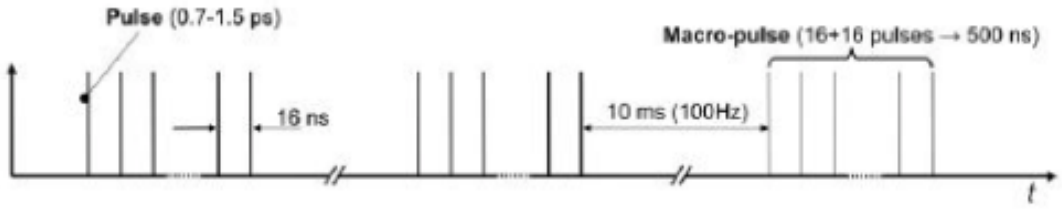

Figure 1.3 - Temporal structure of the GBS gamma beam.

A summary of the main parameters for the electron beam and the laser beam are listed in table 1.2 [12].

Electron beam parameters 32 bunches per RF pulse, 16 ns separation bunch-to-bunch, 100 Hz rep rate	
Mean energy [MeV]	$75 - 750$
Bunch charge [pC]	$25 - 250$
Bunch length [μm] rms	$200 - 300$
Total projected rms transverse emittance x,y [mm·mrad]	$0.3 - 0.5$
Relative rms energy spread [%]	$0.05 - 0.1$
Focal spot size x,y [μm] rms	$15 - 18$
Laser parameters **100 Hz repetition rate**	
Laser pulse energy [J]	$0.2 - 0.4$
Laser wavelength [nm]	515
Laser photon energy [eV]	2.4
Laser pulse length [ps] rms	1.5
Laser focal spot size w_0 [μm]	28
Laser rms bandwidth	< 0.1
Laser M^2	< 1.2
Laser parameter a_0	$0.02 - 0.04$
Collision angle α [^{o}]	172
Laser repetition rate [Hz]	100
Recirculator rate per laser pulse	32

Table 1.2 - Main parameters of the GBS electron and laser beams [12].

Collimation system: as previously stated, ELI-NP-GBS will have two interaction points and associated beam-lines (high-energy and low-energy), that will allow to produce gamma beams in the range 0.2-3.5 MeV and 3.5-19.5 MeV, respectively. The gamma rays emerging

from the two interaction points are not intrinsically monocromatic as it is possible to see from figure 1.4 where the energy distribution of a simulated 3.5 MeV gamma beam produced at GBS is shown [13].

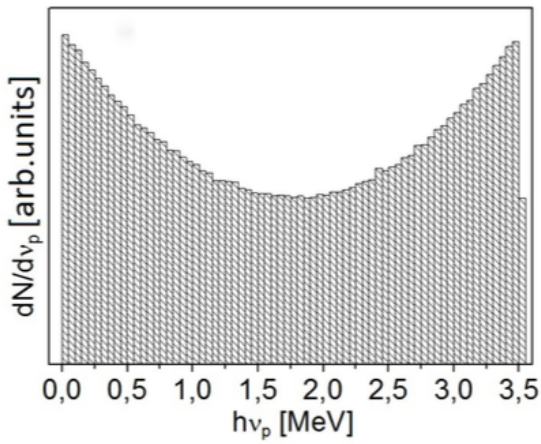

Figure 1.4 - Energy distribution of a 3.5 MeV gamma beam created by inverse Compton effect [13].

The energy of the emitted radiation is strongly dependent on the emission angle: its angular distribution is shown in figure 1.5. As it is possible to see, the energy decreases as the angular propagation increases. In order to obtain a monochromatic spectrum, the photons with a lower energy, emitted at larger angles, must be taken away using an appropriate absorber collimation system. In this way the desidered energies are selected and the bandwidth requirements can be achieved.

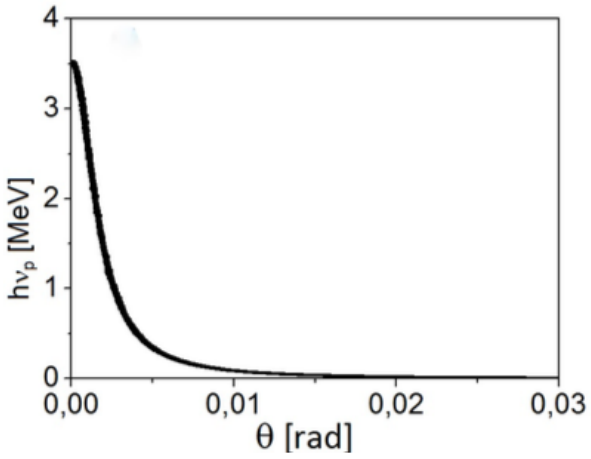

Figure 1.5 - Angular distribution of a 3.5 MeV gamma beam created by ICE [13].

The energy spectrum resulting from a theoretical collimation (by applying a cut on the maximum divergence) is shown in figure 1.6. After the collimation process, the expected GBS gamma beam parameters are the ones reported in table 1.1: a very narrow bandwidth of 0.5% will be combined with a spectral density of the order of 10^4 photons/(s·eV) to form the very intense and brilliant ELI-NP gamma beam.

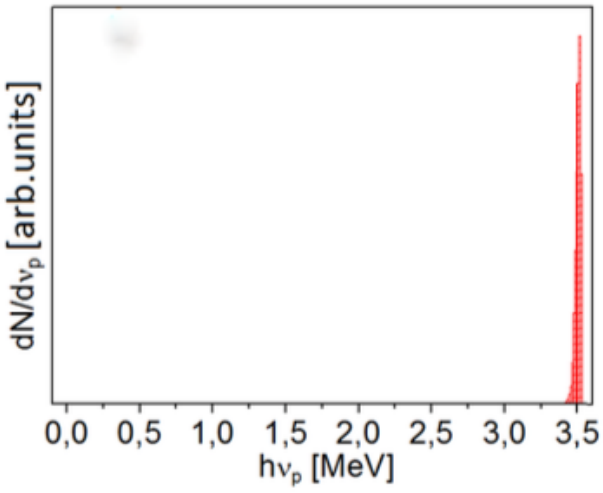

Figure 1.6 - Energy spectrum of a 3.5 MeV gamma beam after collimation [13].

The main requirements for the collimation system are [14]:

- effective attenuation of the gamma radiation;
- continuously adjustable aperture, adaptable to the required maximum energy and bandwidth;
- minimum contamination of the downstream experimental area with scattered radiation.

Moreover, depending on the energy, the angular acceptance required for a relative bandwidth $\Delta E/E=0.5\%$ is between 70 and 700 μrad, which translates in apertures ranging from about 1 to 14 mm [15].
The collimator configuration capable of satisfating the aforementioned requirements resulted to be a stack to be placed along the beam axis of 14 slits with aperture independently ajustable (0-25 mm), mounted on a high precision stainless steel frame.
The slits, composed of two 40 x 40 x 20 mm^3 blocks made of a 97% tungsten alloy, are divided in 3 groups of 4 slits plus 2 additional slits positioned 20 cm aparts from the previous ones to further clean the beam halo (figure 1.7). All of them are aligned along the primary beam with different rotation angles: the aim is to create a collimated gamma beam of octagonal shape, as shown in figure 1.8 [14].
The collimation system is located inside a vacuum chamber equipped with a system capable of controlling with high accuracy the alignment of the chamber in the tranversal directions, pitch and yaw. A concrete wall shields the characterization line and the experimental areas downstream of the collimation from the secondary radiation due to the interaction of the primary gamma beams with the collimator [14].
In figure 1.9 the assembled collimation system (a) is shown along with the vacuum chamber (b) and a 3D model of the complete system (c).

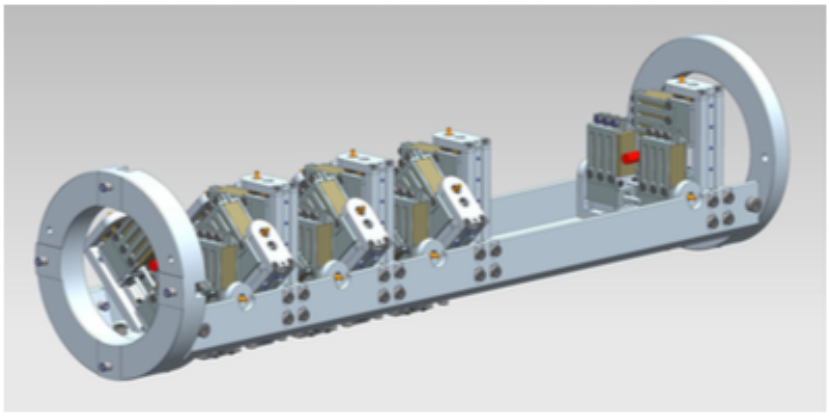

Figure 1.7 - 3D model of the collimation system.

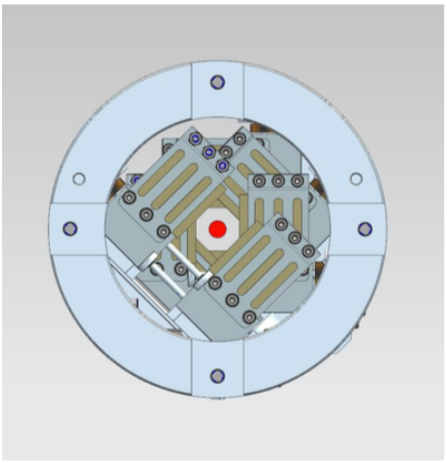

Figure 1.8 - Octagonal shape of the collimation system

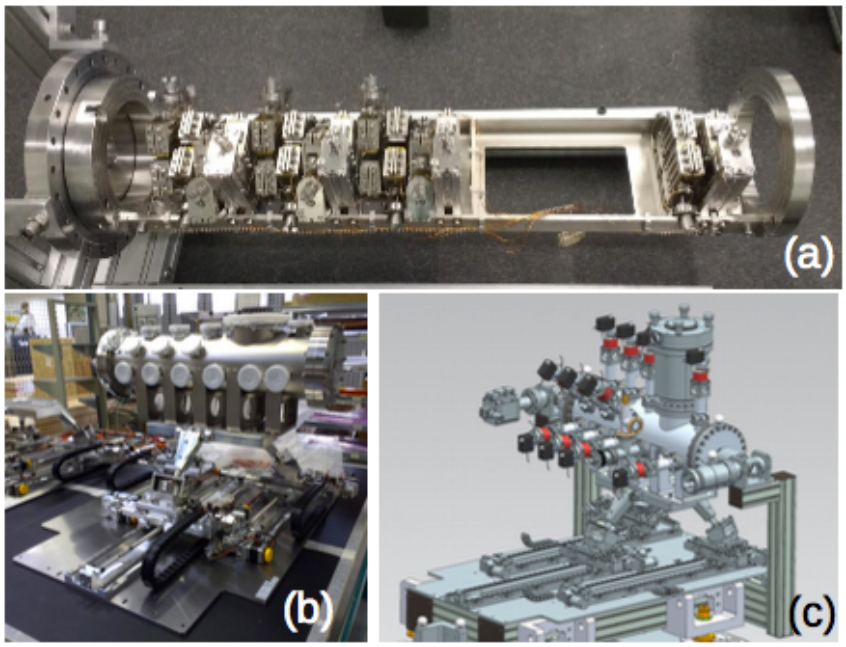

Figure 1.9 – The collimation system assembled, before the insertion in the vacuum chamber (a); the vacuum chamber mounted on top of the SpaceFab positioning system (b); a 3D model of the complete collimation system (c).

The optimal configuration and the performance of the designed collimation system has been evaluated in detail through a dedicated Geant4 application that simulates the transport of the gamma beam from the IP to the experimental area downstream the collimation system [14]. Results have shown that the required energy bandwidth (0.5%) can be attained using this system.

1.3.4 GBS Characterization System

A characterization system providing a measurement of the energy spectrum intensity, space and profile of the beam is essential for the commissioning and development of the source, as well as to demonstrate the performance achieved. A precise energy calibration of the gamma beam and a continuous monitoring of the stability of its parameters during its operation are also necessary for the development of the ELI-NP physics program. According to the beam specification reported in Table 1.1, the required resolution on the energy measurement should not be worse than the expected bandwidth of 0.5% for photon energies up to 20 MeV. Furthermore, the very short duration of the gamma pulse prevents from easily

disentangle the response to each single pulse by using any traditional gamma spectroscopic detector directly exposed to the beam.

To accomplish this task the Gamma Beam Characterisation system designed by the EuroGammaS collaboration will be made by a dedicated system of four detectors: a Compton spectrometer (CSPEC), to measure and monitor the photon energy spectrum; a sampling calorimeter (GCAL) for a fast combined measurement of the beam average energy and its intensity; a nuclear resonant scattering system (NRSS) for absolute beam energy calibration and inter-calibration of the other detectors; a gamma beam profile imager (GPI) to be used for alignment and diagnostics purposes.

Two complete caracterization systems will be delivered for the two γ-beam lines of ELI-NP. The two systems will be almost identical, except for minor design and experimental solutions optimized for the different energy ranges. An overall view of the LE line system is shown in Fig. 1.10.

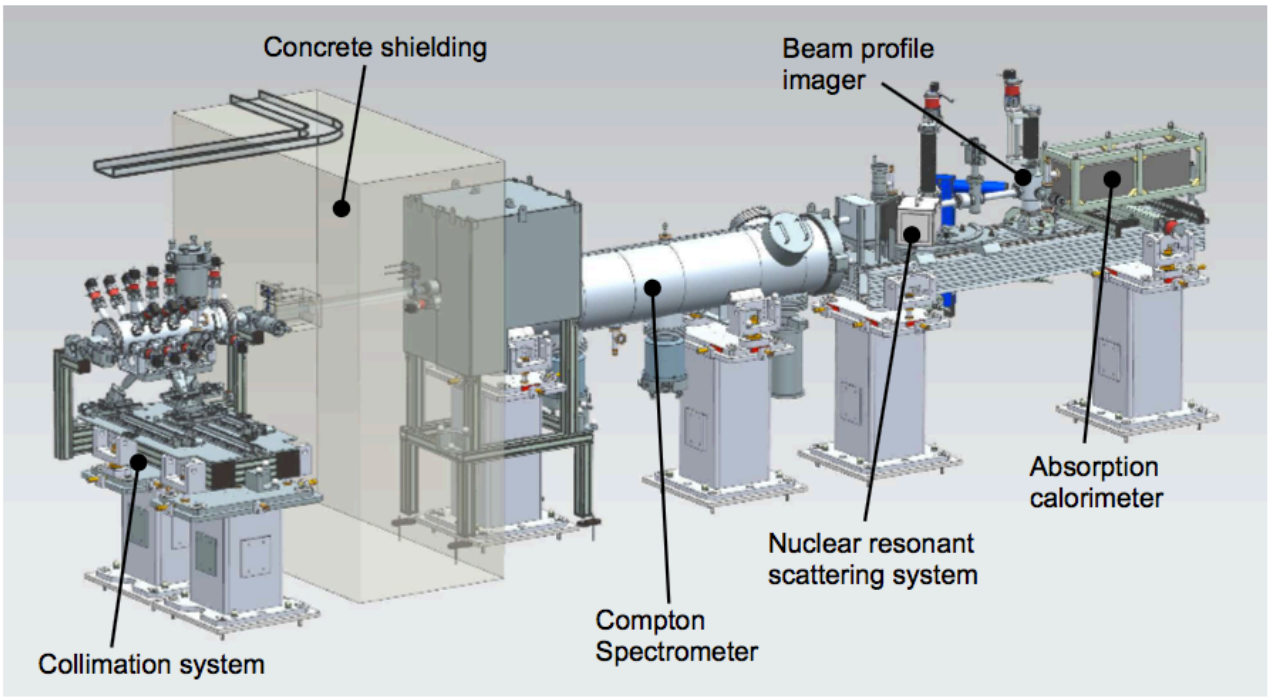

Figure 1.10 – Sketch of ELI-NP-GBS characterization and collimation line

As it is possible to see, the gamma beam enters from left through a concrete shielding block, placed between the collimator and the characterization system, and moves downstream to the various subsystems before reaching the experimental area.
An overview of each component of the characterization system is given below.

Compton spectrometer (CSPEC): The aim of the Compton spetrometer (CSPEC) is to reconstruct the γ-energy spectrum with a non destructive method, suitable for both beam characterization during the commissioning phase and beam monitoring during routine operations of the ELI-NP facility. The basic idea is to measure the energy and position of electrons recoiling at small angles from Compton interactions of the γ beam on a thin Mylar target with thickness ranging from 2 to 100 μm [16].
The electron energy is measured with a hyper-pure germanium crystal (HPGe) positioned two meters downstream of the interaction point at 60 mrad below the beam line. To enhance the full energy peak of the measured electrons while reducing pile up, only particles entering the inner part of the detector are selected using a collimator placed in front of the detector.
Placed between the collimator and the HPGe, a double sided silicon strip detector will determine the impact point of the e^- providing the electron scattering angle θ with a precision better than 1 mrad.
The recoil photon is detected outside the vacuum by Barium Fluoride (BaF_2) crystals, whose fast response in coincidence with the HPGe signal will provide the trigger of the system. The request of a hit in the Si strip strongly reduces the events due to a Compton photon, while the detection of a recoil gamma-ray in coincidence suppresses the background due to pair production inside the target. For all the simulated energies, more than 99% of the selected events contain an electron generated by a Compton interaction in the target.
The BaF_2 crystals are arranged in a small calorimeter of 4×4 crystals. Their size is 1.2×1.2×5 cm^3 and they are read out by a

multianode PMT manufactured by HAMAMATSU (H12700A-3 model). Signals are acquired with a CAEN V1742 switched capacitor digitizer working at a sampling rate of 1 GS/s.

The CSPEC is expected to reconstruct the gamma beam energy spectrum with a relative uncertainty, from about 0.3% at 1 MeV down to 0.1% at 3 MeV for the beam peak energy. The estimated relative uncertainty on the beam width, after deconvolution from the experimental resolution, is 0.2%-0.4% in the same energy range [16]. The main components and the working principle of the Compton spectrometer are illustrated in Figure 1.11.

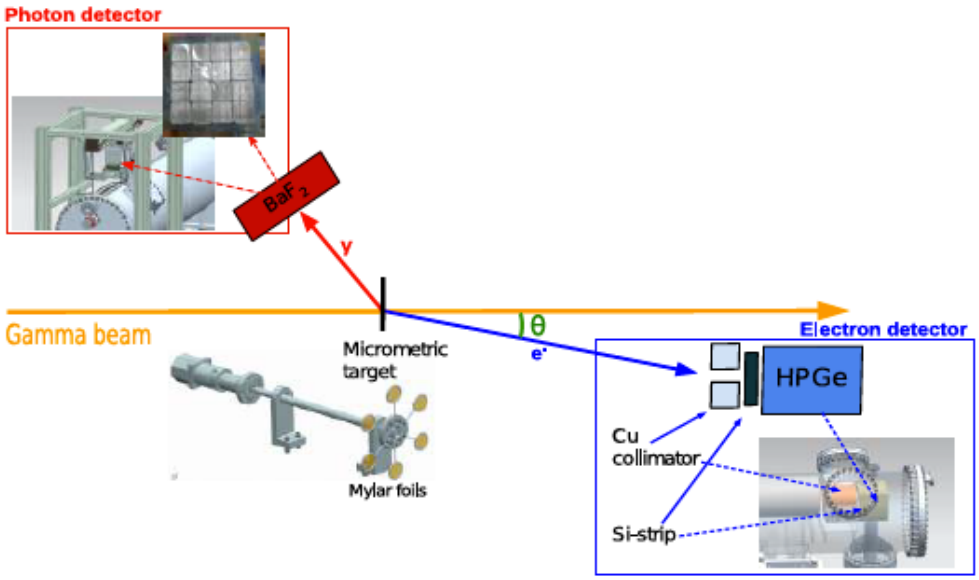

Figure 1.11 - Schematic view of the main components of the Compton spectrometer [16].

The need to use detectors with very high energy resolution, such as HPGe, prevents to perform this measurement on a time scale shorter than the macro-pulse length, resulting in a low rate of clean measurements ($\ll$ 100 Hz).

A complementary approach consists in performing a measurement of the total beam energy by absorbing the gamma pulses in a longitudinally segmented calorimeter.

Absorption Calorimeter (GCAL): The Absorption Calorimeter (GCAL) is designed to measure the total intensity and the average energy of the gamma beam by exploiting the energy dependence of the gamma absorption cross-section for low-Z materials. The detector makes a destructive measurement, so it can not be used during normal data taking, but can provide a fast feedback during the commissioning phase, including the ability to detect instability of the beam energy and intensity within a macro-pulse.

The chosen design for the LE beamline is a sampling calorimeter composed by 22 identical layers. Each element consists of a block of polyethylene absorber (an inexpensive and easily workable low-Z material) followed by a readout board hosting seven adjacent silicon detectors. The chosen Si-strip sensors are processed from n-type phosphorous doped wafers, 320 mm thick, segmented in 128 p+ strips. Figure 1.12 shows on the left a schematic layout of the entire calorimeter and on the right a picture of a single GCAL layer [16].

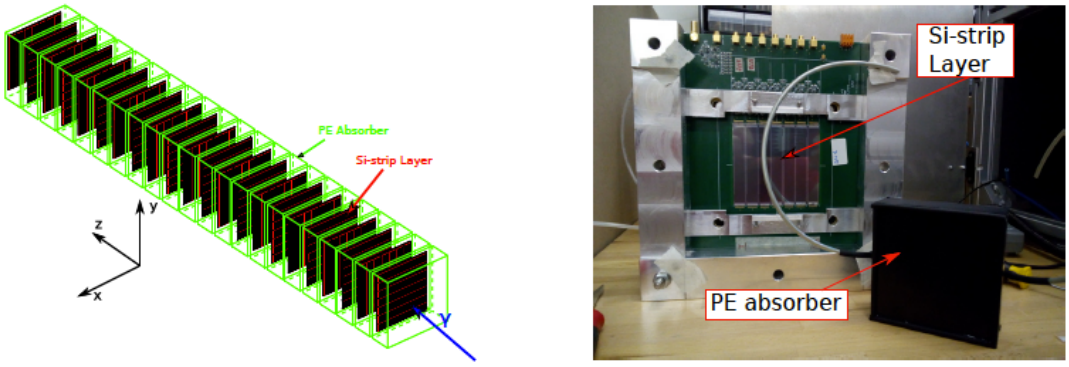

Figure 1.12 - Schematic layout of the LE calorimeter (left); and a picture of a single GCAL layer (right). [16]

This approach relies on the high intensity and monochromaticity of the gamma beam: the longitudinal profile of the energy released by photons in a low-Z and light absorber has a rather strong dependence on the incident photon energy in the operation range of the ELI-NP beam (1-20 MeV) , while the profile fluctuations

are suppressed by the high number of photons. Once the gamma average energy is obtained from the longitudinal profile, the beam intensity is also measured at the same time from the total energy release.
The advantage of this approach is that the full photon statistics can be exploited. Also, since fast detectors can be used, the measurement can be performed for every single pulse allowing it to be used during the machine commissioning and tuning, to check the beam energy and intensity and their variation within a macro-pulse.
The combination of the measurement performed by the Compton Spectrometer and the Absorption Calorimeter will make possible to fully characterize the gamma beam energy distribution and intensity with the precision needed to demonstrate the achievement of the required parameters.

Nuclear Resonant Scattering System (NRSS): The aim of the Nuclear Resonant Scattering System (NRSS) is to perform an absolute energy calibration of the CSPEC and the GCAL devices using the Nuclear Resonant Scattering method. The idea is to detect the resonant gamma decays of properly selected nuclear levels whenever the gamma beam overlaps one resonance level of a target material. Such calibration is performed using appropriate targets characterized by gamma de-excitation emission spectra well known from available literature, so to have a highly accurate measure.
The detection setup has been designed in order to measure nuclear resonance scattering from γ-beam photons at backward angles (around $\theta=135^{\circ}$) with respect to the beam direction as shown in figure 1.13. This angular condition is important in order to reduce the background contribution coming from the target due mainly to Compton scattering.
The mechanical design, presented in figure 1.13, is mainly composed by three parts, namely the scattering chamber, the target holder and the γ-detector, which is placed outside the vacuum line.

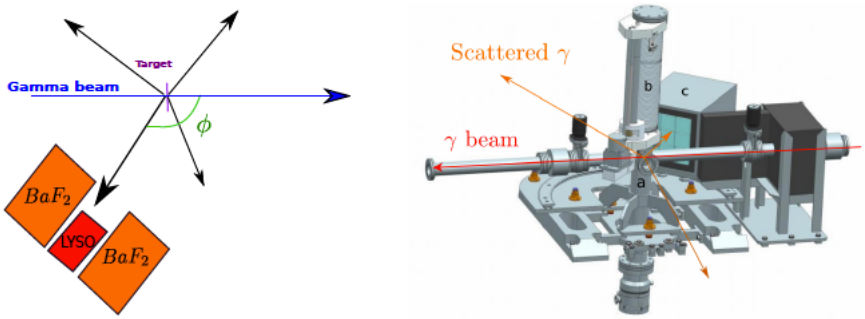

Figure 1.13 - Left figure shows a schematic representation of the NRSS. The right one presents the layout of the NRSS: (a) the scattering chamber; (b) the vertical target shifter; and (c) the scintillators crystal for the g detector. [16].

The γ-detector was designed to work in two different modes: Fast Counter Mode (FC) allows a fast beam energy scan, giving prompt information about the establishment of a resonance condition; and Energy Spectrum Mode (ES) permits the precise identification of the resonant level through the measurement of the energy of the emitted de-excitation photon.

The detector consists of a Lutetium-yttrium oxyorthosilicate (LYSO) crystal of dimensions 3×3×6 cm^3 surrounded by an ensemble of four 5×5×8 cm^3 BaF_2 scintillators. These act both as fast counters for the FC mode and as Compton shield for the ES mode, while the LYSO provides the energy of the γ. The system is placed inside a box with 2 cm-thick lead screen on its side walls [16].

Gamma Profile Imager (GPI): The gamma profile imager (GPI) has the task to acquire images of the spatial distribution of the gamma beam. These images will be used to check the alignment and operation of the collimation system and measure the spatial distribution of the radiation emitted, allowing to verify the size and uniformity of the gamma beam.

In Fig. 1.14 a schematic representation of the imager is shown: it is mainly composed of a scintillator screen placed at 45° degrees with respect to the gamma beam direction, a CCD camera and a lens

system to focus onto the CCD camera the scintillation light created by the interaction between the incident gamma-rays and the scintillator.

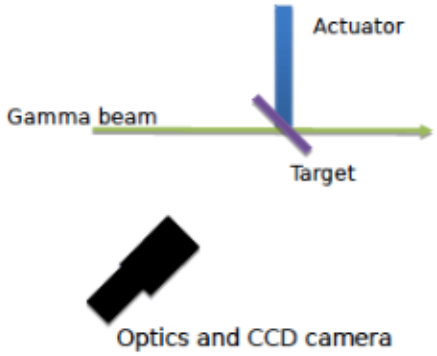

Figure 1.14 - Schematic representation of the Gamma Profile Imager [17].

A more detailed description of the GPI is given in chapter 3.

CHAPTER 2

THEORETICAL BACKGROUND

The present chapter describes the theoretical background and the physical principles underlying the interaction of gamma radiation with matter along with the inverse Compton scattering process. In the second part an overview of the main characteristics of inorganic scintillators is given followed by a description of the properties of CCD cameras and thin lenses. Finally, a brief description of the method used to measure the spatial resolution is given.

2.1 - Interaction of gamma photons with matter

Gamma rays, or gamma radiation, constitute the highest frequency, shortest wavelength end of the Electromagnetic Spectrum. They are emitted by unstable nuclei in their transition to the ground state from the excited ones wich are formed either in the processes of radioactive decay or in nuclear reactions.

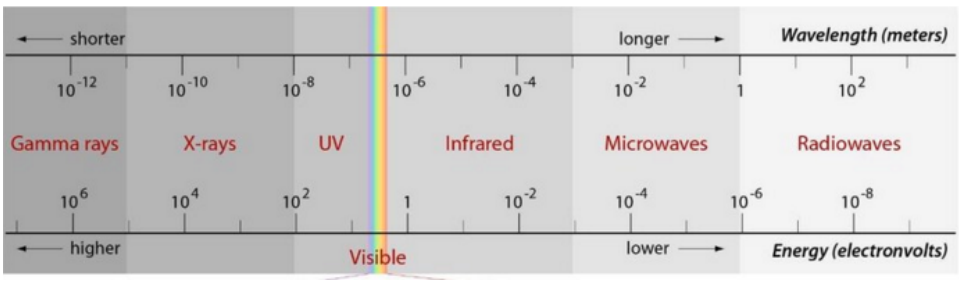

Figure 2.1 - The electromagnetic spectrum from lowest energy/longest wavelength (at the right) to highest energy/shortest wavelength (at the left).

Being gamma rays the most penetrating and energetic electromagnetic radiation, they can travel significant distances through solid material and, in doing so, they interact with electrons or nuclei of the material producing ionization.
The main mechanisms of interactions of gamma-rays in matter are:

- The photoelectric effect, where the energy of the incoming photon is absorbed by an atomic electron that will be ejected from the atom.
- Compton scattering, where the incoming photon loses part of its energy being transferred to an electron.
- Pair production, where the photon converts into an electron-positron pair in the presence of a Coulomb field.

Below, a description of these processes is given.

2.1.1 Photoelectric effect

The photoelectric effect involves the absorption of a photon by an atomic electron which is then ejected from the atom. This can occur only when the incoming photon has an energy hν equal or higher than the binding energy of the electron.
Since an atom is much more massive than an electron, the ejected electron takes practically all the energy and momentum of the photon. The kinetic energy K of the ejected electron is then [18]:

$$K = h\nu - EB \tag{2.1}$$

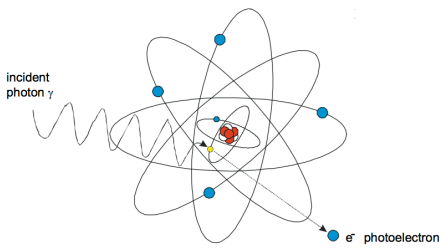

Figure 2.2 - Schematic representation of photoelectric effect: a photon undergoes an interaction with an absorber atom in wich the photon completely disappears. In its place, an energetic photoelectron is ejected from one of the bound shells of the atom [21].

The photoelectric interaction creates a vacancy in one of the electron shells, typically the K or L. This vacancy is filled by the electrons from the higher shells through radiative and non-radiative processes. In the radiative process, the difference in energy between the shells will be emitted in the form of x-ray photons. The process is known as x-ray fluorescence and it is significant for high Z target materials. In the case of non-radiative process, the difference in binding energy between the shells will be transferred to one of the orbital electrons of the outer shell and subsequently the electron will be ejected out. Such electron is known as the Auger electron and the process, significant in low Z target atoms, is known as the Auger process.
The photoelectric interaction cross section is inversely proportional to the gamma photon energy and proportional to the atomic number Z; an approximated formula is given by:

$$\sigma_{ph} = \frac{CZ^n}{(h\nu)^m} \tag{2.2}$$

where m ranges from 1 to 3 and n ranges from 4 to 5. Therefore, the photoelectric effect is dominant mode of interaction for low energy gamma or X-ray photons and significant for absorption material of high atomic number.

2.1.2 Compton scattering

Compton scattering is the interaction between an incoming photon and a free electron at rest. This process dominates when the energy of the gamma photon is in the range 100 keV - 10 MeV. Typical configuration of the Compton scattering is depicted in figure 2.3.

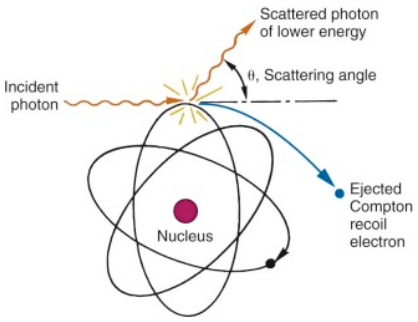

Figure 2.3 - Schematic representation of Compton scattering: the incident photon transfers part of its energy to a Compton recoil electron and is scattered in another direction of travel (θ, scattering angle) [19].

The incoming gamma photon is deflected through an angle θ with respect to its original direction and it transfers a portion of its energy to the electron. As the photon energy is higher than the electron binding energy, the latter can be ignored and the electron can be considered essentially free. By applying energy and momentum conservation, the relation between the gamma energy before (hν) and after (hν′) the collision and the kinetic energy of the scattered electron T can be written as follow [19]:

$$h\nu' = \frac{h\nu}{1+\frac{h\nu}{m_e}(1-\cos\theta)} \tag{2.3}$$

$$T = h\nu - h\nu' = h\nu\left(1 - \frac{1}{1+\frac{h\nu}{m_e}(1-\cos\theta)}\right) \tag{2.4}$$

Because all scattering angles are possible, the energy transferred to the electron can vary from zero to a large fraction of the gamma-ray energy. The maximum kinetic energy that a Compton scattered electron can acquire results from a "head-on" collision which happens when the gamma photon is scattered backwards (θ = 180°). This value corresponds to the Compton edge. The resulting 'ideal' spectrum of a monochromatic beam whose photons undergo only Compton scattering is then given by a continuum distribution, going from 0 to the 'Compton edge', which is always lower than the incident photons energy.

The cross section of this process is described by the well-known Klein-Nishina formula. Probability of finding a scattered photon in a given solid angle along θ is:

$$\frac{d\sigma}{d\Omega} = \frac{r_0^2}{2}\left(\frac{h\nu'}{h\nu}\right)^2\left(\frac{h\nu'}{h\nu} + \frac{h\nu}{h\nu'} - sin^2\theta\right) \tag{2.5}$$

where r_0 is the classical electron radius. In the case in which the energy of the scattered photon is not changed with respect to the energy of incident photon, then one observes elastic scattering. In this situation cross section is independent from the energy and it is equal to the Thomson scattering cross section:

$$\frac{d\sigma_\theta}{d\Omega_\theta} = \frac{r_0^2}{2}(1 + cos^2\theta) \tag{2.6}$$

2.1.3 - Pair production

In this process the incident photon, interacting with the electric field of an atomic nucleus, converts its energy into the mass of an electron-positron pair.

This process is energetically possible only if the gamma-ray energy exceeds twice the rest-mass energy of an electron (1.02 MeV) and becomes important as an absorption mechanism at energies over 5 MeV.

Because the positron will subsequently annihilate after slowing down in the absorbing medium, two annihilation photons are normally produced as secondary products of the interaction [19].

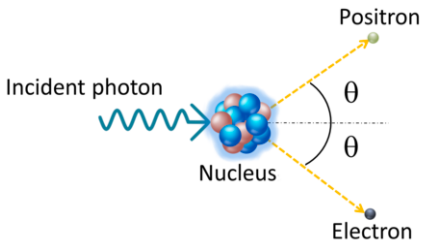

Figure 2.4 - Schematic representation of pair production mechanism [19].

2.1.4 - The total photon attenuation

The total interaction probability for a photon propagating in matter is the sum of the individual interaction probabilities associated with the photoelectric, Compton and pair production interaction mechanisms [19]. As consequence of such kind of interactions a photon that interacts with the target is completely removed from the incident beam, in other words a beam of photons that crosses a medium is not degraded in energy but only attenuated in intensity.

The attenuation of the incident beam is exponential with the thickness of the absorbing medium and can be expressed by the following relation:

$$I = I_0 e^{-\left(\frac{\mu}{\rho}(E)\right)(\rho X)} = I_0 e^{-\mu(E)X} \tag{2.7}$$

where:

- I is the attenuated gamma-ray beam intensity;
- I_0 is the incident gamma-ray beam intensity;
- μ(E) is the linear attenuation coefficient of the absorber for the gamma photon energy E;
- μ/ρ(E) is the mass attenuation coefficient of the absorber for the gamma photon energy E;
- X is the thickness of the absorbing material;
- ρ is the density of the traversed material.

Attenuation properties of absorbing materials are typically expressed in terms of the mass attenuation coefficient μ/ρ (cm^2/g). From the graph of the mass attenuation coefficient as function of the photon energy (figure 2.5) it is possible to notice that the photoelectric effect, Compton scattering and pair production are the dominant interaction mechanisms at low (E_γ<0.1 MeV), medium (0.1<E_γ<10 MeV) and high (E_γ>10 MeV) gamma energies respectively [19].

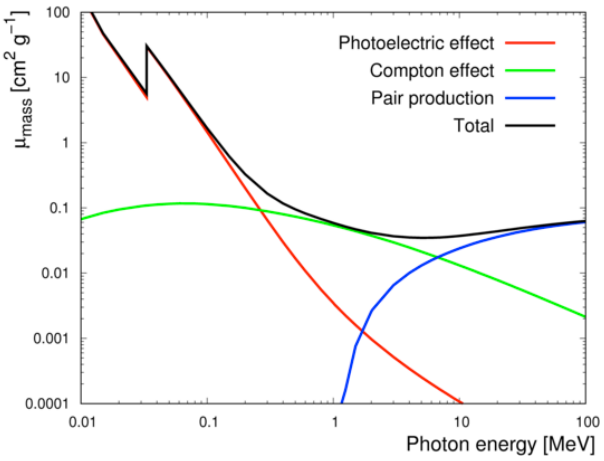

Figure 2.5 - Mass attenuation coefficient as a function of photon energy [19].

2.2 - Inverse Compton source

As stated in the previous chapter, the gamma ray source at ELI-NP will be produced through the inverse Compton interaction between accelerated electrons and gamma photons. In the following sections a description of inverse Compton process is presented and its use as gamma rays source is explained.

2.2.1 Inverse Compton and Thomson back-scattering

Inverse Compton refers to the case in which the scatter of the photon occurs in a reference frame where the electron is not at rest but has a relativistic speed and an energy higher than the one of the interacting photon. In this process it is possible that the photon gains energy in the interaction, for this reason it is usually called inverse Compton scattering[9].

Consider an interaction as depicted in figure 2.6 where an electron is moving with an energy E_e and a photon of initial energy $h\nu$, that propagates toward the electron at an angle θ_i, after the interaction is scattered at angle θ_f with an energy $h\nu'$ [20].

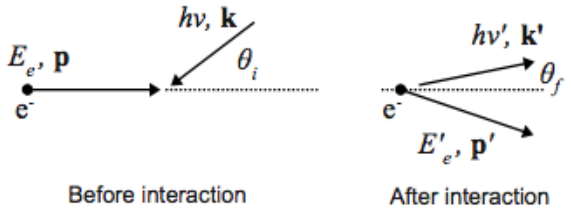

Figure 2.6 - Schematic configuration of inverse Compton scattering.

In the rest frame of the electron the process can be described as a Compton scattering for a photon that has undergone an energy up-shift due to the relativistic Doppler effect. Considering the electron having a Lorentz factor γ, the up-shifted energy $h\nu_*$ will be $h\nu_*=2\gamma h\nu_i$. Thus, in this reference frame a Compton interaction will occur with the photon with the energy $h\nu_*$, but, in order to obtain the description of the process in the laboratory frame of reference, a Lorentz transformation from the electron rest frame must be performed.

Assuming the collision geometry sketched in figure 2.6, where E_e, p and E'_e, p' are the energy and the momentum of the electron before and after the collision while $E_\gamma=h\nu$, k and $E'_\gamma=h\nu'$, k', denote the energy and the wave vector of the photon before and after the collision, using conservation of four-momentum it is possible to write E'_γ as [20]:

$$E'_\gamma = h\nu' = E_\gamma \frac{(1-\beta\cos\theta_i)}{1-\beta\cos\theta_f + \frac{E_\gamma}{\gamma m_e}(1-cos\theta_p)} \tag{2.8}$$

where γ is the Lorentz factor of the relativistic electron and m_e is its mass at rest (511 keV); θ_i and θ_f are the angles between the momentum of the incident and scattered photon with respect to the direction of motion of the electron ($cos\theta_i=p\cdot k$ and $cos\theta_f=p\cdot k'$) and θ_p is the angle between the two photons ($cos\theta_p=k\cdot k'$).

Considering an head-on collision ($\theta_i=\pi$), denoting with θ the angle of the scattered photon, it is possible to rewrite eq. 2.8 as:

$$E'_\gamma = h\nu' = E_\gamma \frac{(1+\beta)}{1-\beta\cos\theta + \frac{E_\gamma}{\gamma m_e}(1-cos\theta)} \tag{2.9}$$

In the case of a collision of a relativistic electron and a photon having an up-shifted energy $h\nu^*$ that is negligible compared to the electron rest mass m_e, it is possible to consider that the interaction in the electron frame of reference is basically a classical Thomson scattering. This means that the electron does not recoil and the photon is reemitted with unchanged frequency corresponding to the original one Doppler up-shifted. In this case, the result in the laboratory frame of reference is a Lorentz boosted Thomson emission, where the scattered photons are peaked along the direction of motion of the electron in a cone with aperture proportional to 1/γ due to the effect of the Lorentz transformation. When this approximation is valid the process is described as Thomson backscattering and the energy of the photon scattered at small angles θ can be expressed with good approximation when $\gamma \gg 1$, as [20]:

$$E'_\gamma = h\nu' \approx E_\gamma \frac{4\gamma^2}{1+\gamma^2\theta^2} \tag{2.10}$$

From equation 2.10 it is possible to notice that the maximum energy E_γ^{max} is obtained for $\theta=0$ and it is equal to $E_\gamma^{max} \approx 4h\nu\gamma^2$.
In this case it is worth noting that the final energy boost factor comes from two consequent relativistic Doppler up-shift between the laboratory and the electron reference frame, each of those gives a boost of a factor $\gamma(1+\beta) \approx 2\gamma$ for $\beta \sim 1$.
In the practical case of a photon having an initial energy hν=2.4 eV, the backscattering with an electron having a γ=145, corresponding to an energy E_e~74 MeV, would result in an energy $h\nu' = 4E_\gamma\gamma^2$ = 0.2 MeV; otherwise, if the 2.4 eV photon interacts with a 728 MeV electron (γ=1425), the resulting maximum energy for the back-scattered gamma beam is equal to 19.5 MeV. It is worth

noting that it is possible to obtain a maximum energy of the backscattered radiation ranging from 200 keV to 19.5 MeV using a visible light photon and just varying the electron beam energy. The scaling of the backscattered energy with γ^2 makes it possible to reach high values with electron beam having energies that are easily obtainable at the state of the art of particle accelerators technology.

2.2.2 Inverse Compton Source features

It is possible to summarize the characteristics of a radiation source obtained by an inverse Compton interaction (Thomson backscattering) of laser light with a relativistic electron beam, as [20]:

- **monochromaticity**: the emission is peaked in a cone with an aperture proportional to 1/2. The maximum energy is obtained in the backward direction and the energy decreases by increasing the angle: this implies that varying the angular acceptance by collimating the beam it is possible to adjust the energy bandwidth of the source;
- **energy tunability**: the maximum energy is proportional to $4\gamma^2$ (in the case of a negligible electron recoil) and to the incident laser wavelength; assuming to keep the laser wavelength constant it is possible to tune continuously the maximum energy of the radiation produced by adjusting the electron beam energy;
- **small focal spot**: the radiation emitting area size is determined by the electron beam cross-section and the laser focusing, typical values are of the order of 10-100 μm;
- **flux**: the number of photons produced per collision roughly scale as [21]:

$$N_{ph} \propto \frac{N_L N_e}{r_L^2 r_e^2} \tag{2.11}$$

so it is possible to increase the number of photons produced increasing the number of laser photons N_L and electrons interacting N_e and decreasing the beam size reducing r_L and r_e (transversal dimensions of the photons laser and of the electron beam respectively), as long as unwanted effects of nonlinearity do not affect the source performance;

- **temporal structure:** the duration of the radiation pulse emitted is directly related to the duration of the pulses of the laser beam and the electron bunches interacting. Thus it is possible to obtain very intense ultrashort radiation pulses (< 1 ps) as well as less intense pulses with a high repetition-rate.
- **polarization:** in the case of Thomson backscattering regime, the polarization of the backscattered radiation is fully controllable by acting on the laser polarization.

2.3 - Scintillator materials

In this section, an overview on scintillator materials is presented with particular focus on inorganic scintillators which are the type considered for the GPI.

2.3.1 - General characteristics

A scintillator is a material with the ability to absorb ionizing radiation, such as x or γ-rays, and to convert a fraction of the absorbed energy into quantum of light. Detecting the location and intensity of this light provides a method for measuring a beam profile.
The relevant properties that contribute to the scintillator material performances are:

- **Sensititivity:** this is the minimum energy that the scintillator has to absorb in order to produce a significant output signal.
- **Energy resolution:** it is the ability of a crystal scintillator to distinguish between gamma rays with slightly different energy.

The energy resolution is defined as the full width of the photopeak at one half of its maximum amplitude (FWHM), divided by the energy of the photopeak, and is typically expressed as a percentage of the peak energy.

- Temporal Resolution: is the time required by the scintillator to produce a response signal. In a scintillator material the temporal resolution is determined by luminescence that is the ability to reemit the absorbed energy in form of visible light. As a first approximation the time evolution of the reemission process may be described as a simple exponential decay [22]:

$$N = \frac{N_0}{\tau_d} e^{(-t/\tau_d)} \tag{2.17}$$

where N is the number of photon emitted in the time t, N_0 is the total number of emitted photons, τ_d is the decay constant. In order to have a signal produced in real time, τ_d has to be as short as possible. In general the light emission from a scintillator crystal occurs by means of two processes:

- fluorescence: is the faster decay mode, it occurs when the singlet excited state decays to the ground state in a time of the order of nanoseconds.
- phosphorescence: is the slower decay mode. Under phosphorescence photons are emitted delayed in time because the excited electron is in a triplet state. Since this condition is not permitted for the selection rules, it is necessary that electron spin flips. Characteristic phosphorescene decay times are of the order of milliseconds.

- Efficiency: absolute (or total) efficiency of a scintillator is defined as the ratio between the number of detected events and number of particles emitted by a source:

$$\varepsilon_{abs} = \frac{N_{det}}{N_{em}} \tag{2.18}$$

In most cases, the total efficiency is given by the product of the intrinsic efficiency ε_{int} and the acceptance (or geometric efficiency) ε_g as showed in equation:

$$\varepsilon_{abs} = \varepsilon_{int} \cdot \varepsilon_g \tag{2.19}$$

The intrinsic efficiency is defined as the ratio between the number of detected photons and the number of incident photons onto the crystal. It depends on the type and on the energy of the used radiation, and on the features of the scintillator material itself.
The geometric efficiency, in contrast, is that fraction of the source radiation which is geometrically intercepted by the detector. This, depends entirely on the geometrical configuration of the detector and source.
- Light yield: a scintillator material that detects particles from a given source accumulates energy that is converted in a luminescent response. The light yield is the term that describes the number of emitted visible photons for the unit of deposited energy in the crystal:

$$LY = \frac{N_{em}}{E_{dep}(keV)} \tag{2.20}$$

In order to give a good luminescent response as a result of interaction with radiation, a crystal scintillator has to satisfy the following requirements:
- high efficiency of conversion of the absorbed energy to fluorescent radiation;
- transparency to its fluorescent radiation in order to allow transmission of the light;
- a short decay time of the induced luminescence so that fast signal pulses can be generated.

In addition, one has to underline that the used crystal scintillator has a characteristic photon emission wavelength and

for this reason, to make full use of the scintillation light, the spectrum should fall near the wavelenght region of maximum sensitivity for the device used to detect the light (CCD camera in this case).
No material meets all these criteria simoultaneasly and a choice of a particular scintillator is always a compromise between these and other factors.

2.3.2 Inorganic Scintillator Crystals

There are two commonly used types of scintillators, inorganic and organic scintillators.
Inorganic Scintillators are crystals grown in high temperature furnaces and are typically Alkali Halides (i.e., NaI, CsI), Oxides (i.e., BGO) or Lanthium Halides (i.e., LaB, LaC) [23].
Organic scintillators are made of organic compounds which are mixed with polystyrene to form a rigid plastic, or with mineral oil to form a liquid. Their most distinctive feature is a very rapid decay time of the order of a few nanoseconds or less.
Whereas the nature of scintillation mechanism in organic materials is molecular, in inorganic scintillators it is clearly characteristic of the electronic band structure found in crystals.
The scintillator materials considered for the target of the GPI are inorganic type. Accordingly, only the scintillation mechanism of materials of such type will be further discussed.

Scintillation mechanism in inorganic crystals:

The scintillation mechanism involved in inorganic crystals begins when the incident ionizing radiation via photoelectric effect, Compton scattering or pair production, depending to the initial incoming energy, excites an electron from the valence band of the solid to the conduction band. When the electron jumps back into the valence band an energy equivalent to the band gap, usually 5 to 10 eV, is released as a photon. It is also possible for the incident radiation to promote a valence electron to an energy

level just below the conduction band called the exciton band. An electron in this state is still electro-statically bound to the hole that it left in the valence band. This electron-hole pair is fairly stable and can migrate throughout the crystal lattice until it encounters an impurity in the crystal structure. At this point the hole left in the valence band can ionize the impurity atom. When a subsequent electron arrives at the impurity it can be trapped by the ion causing the emission of de-excitation radiation.

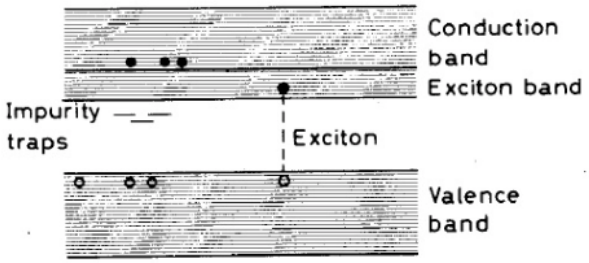

Figure 2.7 - Electronic band structure for inorganic crystals. Besides the formation of free electron and holes, a couple electron-hole is formed; it take name exciton. Exciton can migrate through the crystal and be captured by impurity centers [22].

Inorganic scintillators offer the advantage of an excellent energy conversion and high absorption efficiencies and a good probability for the photoelectric effect compared to organic scintillators. The main disavantage is their response time, 2-3 orders of magnitude higher with respect to the organic crystals, due to phosphorescence.
However, considering the application specific of this project, the response time is not a critical factor as long as it allows to produce an image in a period of one second. On the other hand, the light yeld has to be as high as possible because in this way a good signal will be formed on the CCD.

2.4 Charge Coupled Device (CCD)

A Charge Coupled Device (CCD) is an electronic device used to convert incident light into electrical signals.

The high sensitivity and resolution of these devices combined with their low cost and simple operation make them ideal for measuring the intensity and spatial distribution of scintillation. In the following sections the working principle and the main caracteristics of CCD camera are discussed.

2.4.1 Working principle

CCD consists of a thin silicon wafer divided into millions of tiny light sensitive squares, each square in the pixel grid corresponds to an individual pixel in the final image. When photons hit the silicon surface, they turn into electrical charges through the photoelectric effect and are attracted to the nearby pixel squares. Once the chip has been exposed to an image, charges move between the squares until they reach the charge amplifier. The output voltage is directly proportional to the number of photons that penetrate the tiny squares. This output voltage, which represents the brightness of the image at the corresponding pixel location, is then convert to a digital signal

2.4.2 - CCD Properties

The main parameters used to characterize a CCD camera performances are [24], [25]:

- Spectral sensitivity:

CCDs are not equally sensitive to all wavelengths of light. Spectral sensitivity is defined as the relative efficiency of detection of light as a function of the frequency or wavelength of the signal [26]. It is determined mainly by the material of the CCD, in particular it is worked out from the energy gap E_g.

- Quantum Efficiency QE

Quantum efficiency is the ability of a CCD camera to convert the incoming photons into useful output. It is defined as the fraction of incident photons that are converted into photoelectrons. The QE depends on the wavelength of the incoming photon as shown in figure 2.8. Each CCD has a wavelenght that maximize the conversion

of incoming photon in photoelectron. Therefore, it is important to check that scintillator material emits visible photon with a wavelength compatible with the CCD maximum quantum efficiency.

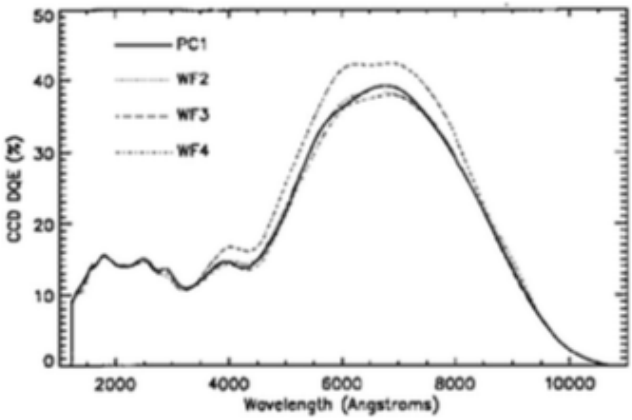

Figure 2.8 - Quantum efficiency chart for a silicon based CCD image sensor.

- Charge Transfer Efficiency

Charge transfer efficiency is the parameter that characterize the efficiency to transfer the photoelectrons from one pixel to the adjacent pixel during a shift operation. If the efficiency is 1, then all the photoelectrons are always transferred without any loss. Normal charge transfer efficiency in scientific CCD cameras is nearby 0,9999999.

- Dark Current DC

Dark current is composed by the electrons that are generated by thermal excitation. A CCD cannot distinguish electrons generated by photons from those generated by heat, therefore dark current adds a random noise to the output signal. This dark noise can be minimized by cooling the CCD to very low temperatures.

- Readout noise RN

Readout noise is another characteristic noise defined as the number of electrons that are added to the signal from the CCD electronics during charge readout.

This noise is measured in e^-/pixel and depends on the size of the amplifier, readout speed (slower readout means lower noise) and on the construction of the integrated circuit.

- Pixel Size

In the definition of pixel size it is necessary to take into account the full well capacity that is the maximum number of electrons that a pixel is able to contain. Pixel of largest size permit to collect more charge and for this reason their full well capacity increases. On the other hand, the creation of too large pixels reduces the spatial resolution. With a little size pixel the spatial resolution improves but the saturation occurs easily. In this situation the CCD is not able to return a linear signal response because of charge overflow from pixels exceeding full well capacity. This effect is called blooming and it affects the entire array.

- Binning

Most CCDs can combine multiple pixel charges to form a single larger charge or superpixel. This super pixel represents the area of all the individual pixels contributing to the charge. This is referred to as binning. For example a binning of 1x1 means that the signal arises from an individual pixel, a binning of 2x2 means that four adjacent pixels have been combined into one larger pixel increasing the area and the sensitivity to light by a factor of four (Figure 2.9). This can reduce exposure times, spatial resolution, however, gets worse as the binning area increases.

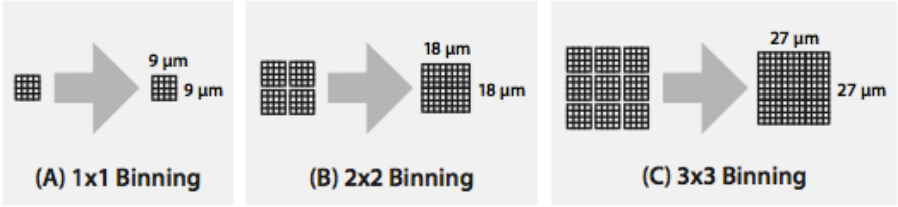

Figure 2.9 - Schematic depicting the mechanism of pixel binning. In 1x1 binning, one pixel is treated as one pixel (A). In 2x2 binning, four pixels are treated as one pixel in order to increase sensitivity and decrease the time for image acquisition, while resolution decreases by a factor of four (B). In 3x3 binning, nine pixels are combined to make one pixel, and resolution decrease by a factor of nine (C) [24].

- Gain G

The Gain G is the number of stored electrons required to produce a digital signal measured in ADU (Analog-to-Digital Unit):

$$G = \frac{N_{e^-}}{ADU} \tag{2.21}$$

Its maximum value is fixed by the number of bits used by the A/D converter and it is 2^n, being n the number of bits.

- Dynamic Range

The dynamic range of a CCD is typically defined as the full-well capacity divided by the camera noise and relates to the ability of a camera to record simultaneously very low light signals alongside bright signals. The ratio is often expressed in decibels or is dimensionless:

$$dyn_{CCD} = \frac{fullwell\ capacity[e^-]}{readout\ noise[e^-]} \tag{2.22}$$

$$dyn_{CCD} = 20log\left(\frac{fullwell\ capacity[e^-]}{readout\ noise[e^-]}\right) \tag{2.23}$$

- Signal to Noise ratio

The signal-to-noise ratio for a CCD camera is the ratio of the total signal to the total noise and can be calculated as follows [27]:

$$SNR = \frac{P \cdot Q_e \cdot t}{\sqrt{P \cdot Q_e \cdot t + D \cdot t + N_R^2}} \tag{2.24}$$

where P is the incident photon flux (photons/pixel/second), Q_e is the CCD quantum efficiency, t is the integration time (seconds), D is the dark current value (electrons/pixel/second) and N_r is the read noise.

2.5 – Optics

In this section the properties of lenses and how they form images are exposed. A brief description of the method used to measure the spatial resolution of an optical system is given in the final subsection.

2.5.1 - Thin lenses

A lens is a transparent medium, usually glass, bounded by two curved surfaces, generally either spherical, cylindrical, or plane. A thin lens is a lens with a thickness negligible compared to the radii of curvature of the lens surfaces.

As illustrated in Fig. 2.10, the line which passes normally through both bounding surfaces of a lens is called the *optic axis*. The point O on the optic axis which lies midway between the two bounding surfaces is called the *optic centre* [28].

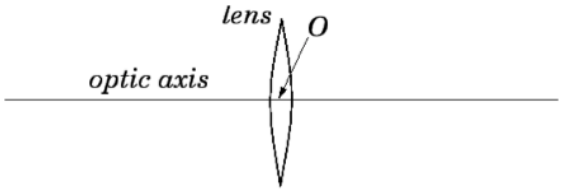

Figure 2.10 – The optic axis of a lens

There are two basic kinds of lenses: *converging*, and *diverging*. A converging lens brings all incident light-rays parallel to its optic axis together at a point F, behind the lens, called the *focal point*, or *focus*, of the lens. A diverging lens spreads out all incident light-rays parallel to its optic axis so that they appear to diverge from a *virtual focal point* F in front of the lens. The differing effects of a converging and a diverging lens on incident light-rays parallel to the optic axis (*i.e.*, emanating from a distant object) are illustrated in figure 2.11.

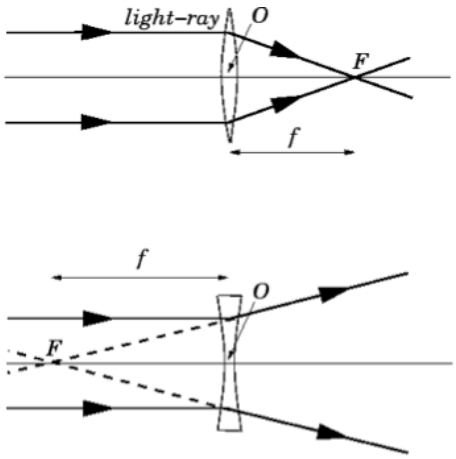

Figure 2.11 – Focus of a convergence (top) and divergence lens (bottom)

The focal length of a lens, which is usually denoted f, is defined as the distance between the optic centre O and the focal point F. The detailed prediction of how images are produced by these lenses can be made using ray-tracing. In figure 2.12 it is possible to see an example for convex and concave lenses.

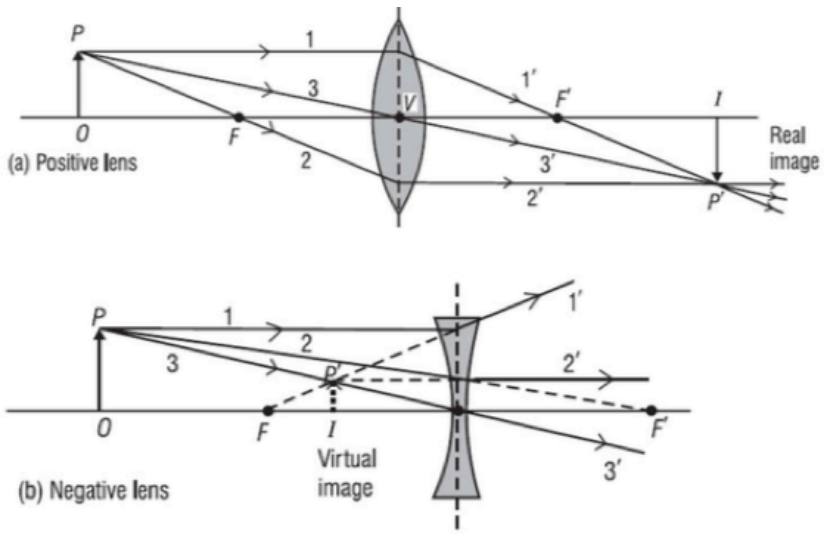

Figure 2.12 - Ray diagrams for image formation by positive and negative lenses

Thin lenses follow a simple equation, derived from a geometric analisys of ray tracing, that relates the object distance p, the image distance q, and the focal lenght f.

$$\frac{1}{p}+\frac{1}{q}=\frac{1}{f} \tag{2.25}$$

The magnification M produced by a thin lens is given by equation 2.26:

$$M=\frac{h_i}{h_o}=\frac{p}{q} \tag{2.26}$$

where h_i is the transverse size of the image, h_o is the transverse size of the object, p and q are object and image distances respectively.

The sign convention to be used in the application of previous equations is:

Light travels initially from left to right toward the lens; object distance p is positive for real objects located to the left of the lens and negative for virtual objects located to the right of the lens; image distance q is positive for real images formed to the right of the lens and negative for virtual images formed to the left of the lens; the focal length f is positive for a converging lens, negative for a diverging lens; the radius of curvature r is positive for a convex surface, negative for a concave surface; transverse distances (h_o and h_i) are positive above the optical axis, negative below.

f-number and Numerical Aperture Of a Lens.

The size of a lens determines its light gathering power and, consequently, the brightness of the image it forms. Two commonly used indicators of this special characteristic of a lens are the f-number and the numerical aperture. The f-number, also referred to as the relative aperture and the f/stop, is defined simply as the ratio of the focal length f of the lens to its diameter D, as given in equation 2.27.

$$f-number=\frac{f}{D} \tag{2.27}$$

For example, a lens of focal length f=4cm stopped down to an aperture of D=0.5cm has an f-number=4/0.5=8. Photographers usually refer to this situation as a lens with an f/stop = f/8.
The definition of numerical aperture is given in equation:

$$N.A. = n \sin \alpha \tag{2.28}$$

where n is the index of refraction of the intervening medium between object and lens and α is the half-angle defined by the limiting ray. Image brightness is dependent on values of the f/number or numerical aperture, in accordance with the following proportionalities:

$$\text{image brightness} \propto 1/(\text{f/number})^2$$

$$\text{image brightness} \propto (\text{N.A.})^2$$

In summary, one can increase the light-gathering power of a lens and the brightness of the image it forms by decreasing the f-number (this means increasing lens diameter). In this case light gathering increases because a wider lens is able to accept more light than a smaller. Increasing the numerical aperture of the lens means an increment of the refraction index that makes possible a larger acceptance angle.

2.5.2 - Spatial Resolution

The ability of an imaging system to resolve small objects is described by its spatial resolution. It is usually defined as a number of line pairs per millimeter, where a line-pair is a sequence of one black line and one white line, that an optical system can resolve.
The measure of line-pairs per millimeter (lp/mm) is also known as frequency. An image with a high lp/mm value is a high spatial frequency image as there are many alternating light and dark regions in a single millimeter.

How well a system is able to reproduce the object spatial frequency is expressed by the modulation transfer function (MTF).

Modulation Transfer Function (MTF)

The modulation transfer function is the response of an optical system to sinusoids of different spatial frequencies [29].
It can be measured by considering a sinewave input signal of increasing spatial frequency and then measuring the contrast in the corresponding output image patterns. Plotting the ratio between the amplitude of the sinusoidal curve on the image and the original sinusoidal curve against spatial frequency will produce the MTF curve as shown in figure 2.13. Its value is always between 0 and 1 (optimal transmission).
The limiting resolution of an optical system is usually defined as the spatial frequency at which the MTF is 3%.

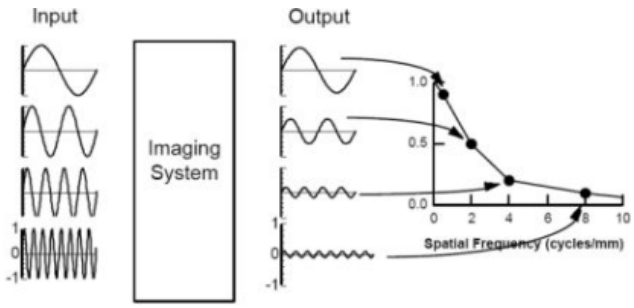

Figure 2.13 - Initial frequency amplitude vs image frequency amplitude. As spatial frequency increas as the system degrade the modulation

Another common way of assessing the intrinsic resolution properties of an imaging system is by measuring the line spread function.

Line Spread Function

A line spread function (LSF) describes the system response to a line pattern [30]. Fig. 2.14 shows the image of a slit wich acts

as a linear source. The variation of light intensity across the image of slit target gives the LSF.

Spatial resolution is conventionally quantified as the full width at half maximum (FWHM) of the Line Spread Function. Different measures are also possible such as the full width tenth maximum.

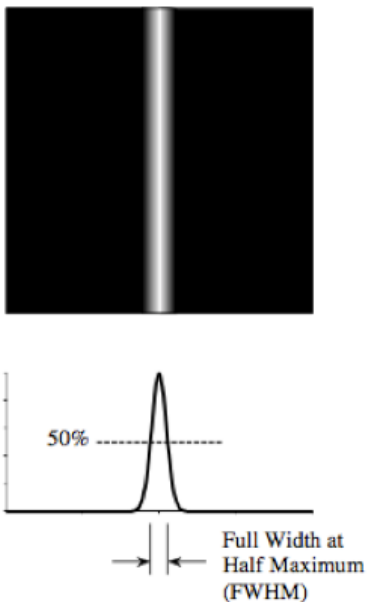

Figura 2.14 - line spread function (LSF) and measured broadening as full width half maximum [28]

CHAPTER 3

DESIGN STUDY AND REALIZATION OF THE GPI PROTOTYPE

In this chapter the design study and development of the Gamma Profile Imager (GPI) is discussed. First the expected performances and requirements are introduced along with the analytical model employed to predict the GPI behaviour. Then the actual GPI design and development process is presented with a detailed description of the various components and the motivations that have brought to the final configuration of the system.

3.1 – Gamma Profile Imager (GPI)

As stated in chapter one, the Gamma Beam System of ELI-NP includes a set of detectors for the diagnostic and the complete characterisation of the gamma beam. To evaluate the spatial distribution of the beam a gamma beam profile imager is required. The adopted system for this purpose, sketched in figure 3.1, consists of a thin scintillator screen, crossed by the gamma beam at an angle of 45°, coupled to a high resolution CCD-camera. Gamma-ray photons arriving from the source interact with the scintillator and generate optical photons wich are subsequently focused by a lens system onto the CCD camera that will be able to produce an image of the gamma beam with a resolution compatible with the beam spot size.

A set of analytical calculations and Monte Carlo simulations were carried out to optimise the imager design and evaluate the performance expected with ELI-NP gamma beam. In the next section the expected performances and requirements of GPI are discussed. A

description of the analytical model adopted is given in section 3.1.2.

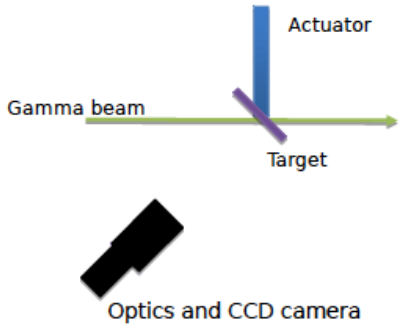

Figure 3.1 - Scheme of the GPI working principle

3.1.1 GPI: expected performances and requirements

The task of the Gamma Profile Imager is to provide an image of the gamma beam spatial distribution. This image is crucial in giving informations on the alignment of the collimation system and on the correct positioning of the other detectors, as well as to control the size and the shape of the γ beam.

As mentioned in chapter one, the designed collimation system will produce beams with an octagonal shape [14]. The GPI will be placed at a distance of 15.2 m (HE line) and 16.3 m (LE line) from the Interaction Point (IP). This implies that the typical size of the beams will vary between about 1 to 11 mm (octagon's apothem), depending on the selected energy and bandwidth.

In Fig. 3.2, 3.3 and 3.4 the beam cross-section expected on the GPI is shown in the case of 3 MeV, 10 MeV and 18.4 MeV gamma beams.

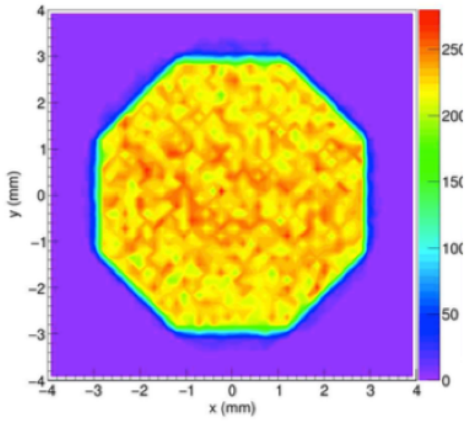

Figure 3.2 - Expected beam spot at 3 MeV

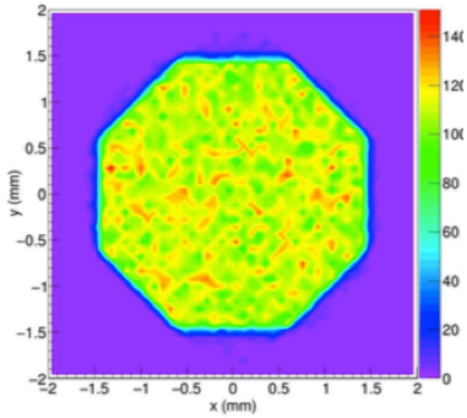

Figure 3.3 - Expected beam spot at 10 MeV

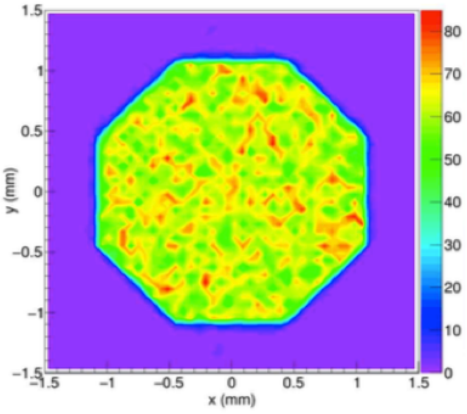

Figure 3.4 - Expected beam spot at 18.4 MeV

Essentially the GPI has to represent on the CCD the same shape profile. If this condition is not achieved, it is possible that the collimator is misaligned as shown in figure 3.5.

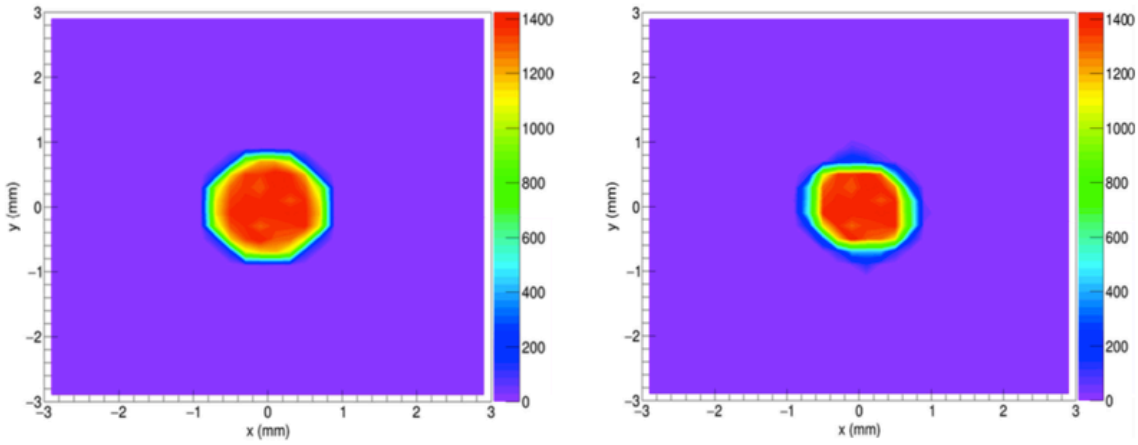

Figure 3.5 - Expected beam spot at 18.6 MeV. (a) Perfect aligned slits. (b) Slit misaligned, σ=100μm [31].

In order to have a profiler that is able to produce such images the following requests have to be satisfied [32]:

- spatial resolution down to 100 μm. From preliminary calculations one expects resolution values of about 100 μm for a long integration time and a little bit worse resolution for a shorter integration time. This level of resolution is necessary in order to distinguish the maximum number of photons that arrives at the CCD with a thin distance from each other. In this way it is possible to depict the beam spatial distribution.

- FWHM of the source image of the order of 1.0 to 10 mm and a source divergence in the range 70-700 μrad in according with the bandwidth specification of the collimation system. These values are valid for source distance of 15 m (high energy line) and 16 m (low energy line);

- time of visible light emission of the order of few seconds or less in order to depict the gamma spot in real time.

Moreover, vacuum compatible materials must be used and particular attention must be payed for operation safety in a radiation environment.

3.1.2 - Analytical model for performance estimation

As stated before, in order to select an acquisition system (lens + CCD) providing the desired performance, a simple analytic model has been developed. The main goal of the model is to work out an expression for the signal expected on the CCD as a function of the system configuration. Fig. 3.6 shows a sketch of the system [32].

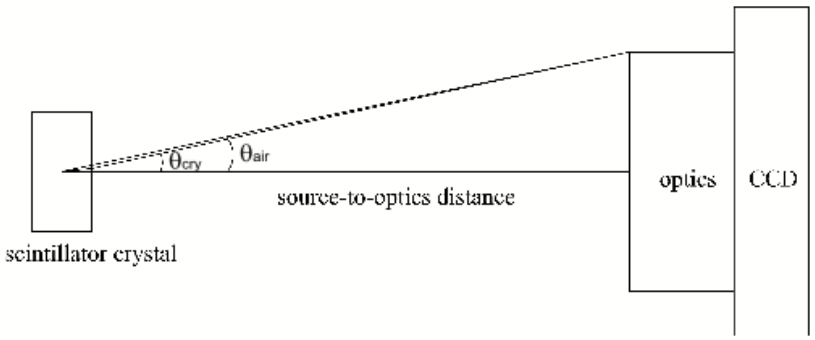

Figure 3.6 - Scheme used to evaluate the signal on the CCD.

A scintillator crystal with light yield Y , thickness t and refractive index n (at the emission peak wavelength) is irradiated by a gamma beam and emits optical photons (ph) which undergo refraction when they exit the crystal. Some of these photons are collected by an optics and focused on a CCD, which convert them in a gray level image.

The mean gray level per second of a pixel of the image can be written as:

$$GL = \frac{E_{dep} Y \varepsilon T c_f \Delta_{CCD}^2}{Am^2} \tag{3.1}$$

where E_{dep} is the energy deposited in the unit of time by the gamma beam in a region of the scintillator of area A, ε and T are the collection efficiency and the transmission factor of the optics respectively, c_f and Δ_{CCD} are the gray level per incident photon conversion factor and the pixel size of the CCD respectively, and m is the magnification ratio of the system, namely the ratio

between image size and object size (in this case, the scintillation spot).
If we make the hypothesis that the scintillator-to-optics distance p is much larger than the crystal thickness and the lens diaphragm diameter D, the small angle approximation can be used and the optics collection efficiency can be written as:

$$\varepsilon = \frac{\Omega}{4\pi} = \frac{1-\cos\theta_{cry}}{2} \approx \frac{\theta_{cry}^2}{4} = \frac{D^2}{16n^2p^2} \tag{3.2}$$

Where θ_{cry} is the refraction angle of the emitted photons.
Moreover, if we use the thin lens expression for the magnification ratio:

$$m = \frac{f}{p-f} \tag{3.3}$$

and introduce the lens F-stop F = f/D, we end up with:

$$\varepsilon = \frac{1}{16n^2F^2}\frac{m^2}{(1+m)^2} \tag{3.4}$$

The CCD c_f coefficient can be written as:

$$c_f = QE \cdot CTE \cdot G \cdot FF \tag{3.5}$$

where QE is the quantum efficiency (e/ph) at the scintillator peak emission wavelength, CTE the charge transmission efficiency, G the electronic Gain (GL/e), and FF the fill factor, namely the ratio of active area and total area of the sensor.
Using Eq. (3.4) and (3.5), Eq. (3.1) becomes:

$$GL = \frac{c_f\Delta_{CCD}^2}{16}\cdot\frac{Y}{n^2}\cdot\frac{E_{dep}}{A}\cdot\frac{T}{F^2}\cdot\frac{1}{(1+m)^2} \tag{3.6}$$

The energy deposited per second inside the scintillator by a gamma beam of energy E can be evaluated via simulation or can be calculated through the following expression

$$E_{dep} = NE\left[\frac{\mu_{en}(E)/\rho}{\mu(E)/\rho}\right](1 - \exp(\mu(E)t)) \tag{3.7}$$

where ρ, $\mu(E)$, and $\mu_{en}(E)$ are the density, the linear attenuation coefficient and absorption coefficient at energy E of the scintillator, respectively and N is the number of photons per second of the beam.

From equation (3.6) it is possible to clearly identify the individual contribution of each system component to the signal on the CCD. As expected, the higher cf and T, namely the quality of the acquisition system, the higher GL, moreover, GL increases if the lens aperture and the CCD pixel size is increased. The factor Y/n^2 accounts for the contribution of the scintillator while the factor E_{dep}/A depends both on the target and the gamma beam to be imaged. The higher the specific energy deposition inside the target, the higher GL. Therefore, the expected signal increases as the mean energy of the gamma beam increases. Finally, GL increases if the chosen magnification ratio decreases.

There are limitations to the range of useful magnification values. The lower bound is due to the required image resolution. In particular, by imposing that a detail of the image with size equal to the object space desired resolution R_{obj} is imaged by at least 2 pixels of the camera, it follows that:

$$m \geq \frac{2\Delta_{CCD}}{R_{obj}} \tag{3.8}$$

On the other hand, if we impose that the scintillator thickness is entirely inside the depth of field of the lens DoF:

$$DoF = 2 \in \frac{p^2}{Df} \geq t \tag{3.9}$$

where $\in$ is the circle of confusion diameter, we obtain the upper bound for m:

$$m \leq \frac{b}{1-b} \qquad b = \sqrt{\frac{2\in F}{t}} \tag{3.10}$$

If we set typical values for the system parameters, namely t=0.5mm, F=2, $\in = \Delta_{CCD}$ =5µm, R_{obj} ≈100µm, we obtain:

$$0.1 \leq m \leq 0.4 \tag{3.11}$$

3.2 – Design study of GPI prototype:

In order to validate the model described in the previous section, a GPI prototype was developed, assembled and tested at INFN Ferrara laboratory.
This section reports the design study of the prototype based on the geometrical constraints and on the following required specifications:

- Significant images in a reasonable time (~ 1 s).
- Spatial resolution down to 100 µm.
- Significant amount of pixels involved in each image.
- Usage of vacuum compatible materials.
- Safe operation in a radiation environment.
- Reconfigurable.

Each component of the detector is presented, with particular focus on the evaluations that led to the final configuration.
In the following, the considerations behind the choice of the target material are discussed.

3.2.1 - Target material selection

The choice of the target material and thickness is the result of a trade-off between conflicting requirements and has been carried out through a set of Monte Carlo simulations.

As stated before, the task of the GPI is to provide a good image of the gamma beam in a short time. In order to have a significant image in a reasonable time the used target should have a good conversion efficiency and therefore high density, high-Z, and feature a good light yield.

Fig. 3.7 shows the light emission obtained with Monte Carlo simulations from various scintillator materials of different thickness in the case of a 3 MeV beam.

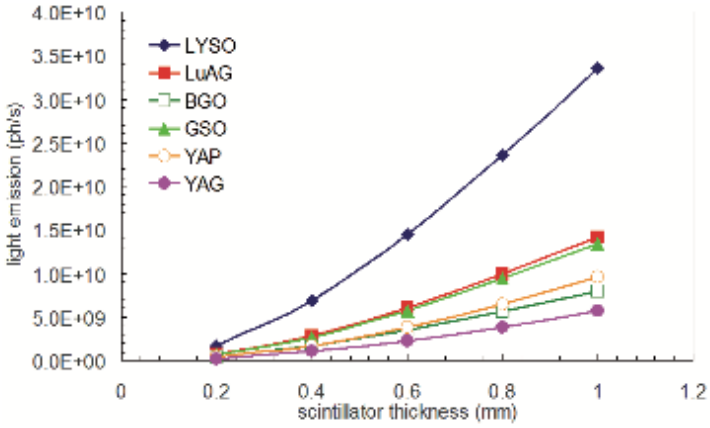

Figure 3.7 - Light emission from various crystals as a functionof thickness for the 3 MeV beam [32].

For each crystal, the total energy released by the gamma beam inside its volume was evaluated from the simulations. Then, the light emission was calculated by multiplying this value by the crystal nominal light yield found in the literature. Moreover, the fraction of light lost due to total internal reflection was taken into account.

From the figure above we can notice that the efficiency is strongly dependent on the target thickness: scintillators emit more light as their thickness increases because the probability of energy deposition is higher. However, the thickness can not be

increased arbitrarily because thicker samples lead to a degradation of the achievable image resolution. This effect is shown in figure 3.8 where the energy deposition distribution inside a LYSO crystal is reported for two different thicknesses and two different energies of the gamma beam. Since, the higher the energy, the smaller the beam cross-section, it follows that the higher energy beams are more affected by the deterioration of resolution. It is also worth noting that, the higher the beam energy, the higher the specific energy deposition inside the scintillator.

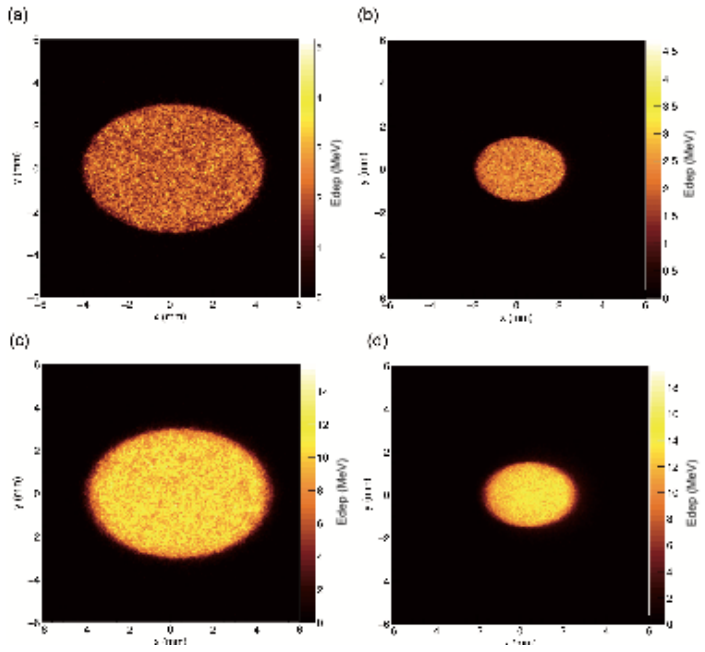

Figure 3.8 - Energy deposition distribution inside a LYSO crystal of different thickness. (a) 300 µm crystal, gamma beam of 3 MeV . (b) 300 µm crystal, gamma beam of 10 MeV . (c) 700 µm crystal, gamma beam of 3 MeV . (d) 700 µm crystal, gamma beam of 10 MeV [32].

From the simulations it comes out that a thickness of 0.5 mm is the best trade-off between light emission and image resolution for the whole gamma beam energy range. However, the target holder will allow to position on the gamma beam crystals of different thickness allowing to suit the image requirements of higher effciency or higher resolution.

Amongst the target requirements, the radiation hardness is an other factor to be considered since it is required that crystal works at nominal parameters and it has to be able to guarantee a continuous use (24h/7, 365days/year) for at least one year without a significant degradation of performance in light yield and transparency.
Moreover, hygroscopicity has to be seriously taken into account because the crystal will be mounted in vacuum and for this reason it is necessary that crystal does not degrades or loses some materials as consequence of air moisture absorption.

From picture 3.7 we can also notice that LYSO resulted by far the material producing more light. Moreover, it is not affected by hygroscopicity and its radiation hardness, compared to the average dose released by ELI-NP-GBS working at the nominal conditions, allows a continuous irradiation for several days without a significant degradation of performance. Therefore, considering the small fraction of time in which the target will be exposed to the beam during a routine use, it is possible to conclude that the degradation of performance due to radiation damage is not critical for several months of usage.
All these facts led us to consider LYSO the ideal candidate for the imaging system.
In order to confirm this result, a characterization test, descripted in the following section, was performed on a $35x35x0.5mm^3$ LYSO sample.

- Characterization of LYSO scintillator
The aim of this test was to investigate the energy resolution and the LYSO light output response to gamma ray excitacion and compare the acquired data with simulations.
The tested crystal, shown in figure 3.9, was a Cerium-doped LYSO scintillator with chemical formula $Lu_{1.9}Y_{0.1}SiO_5$: Ce(0.5%) produced by Epic-Crystal. Its characterstics, extracted from the datasheet

provided by the manufacturer and various sources in the literature, are reported in table 3.1 [33],[34],[35].

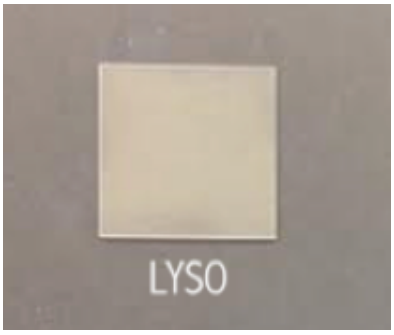

Figure 3.9 – The tested LYSO crystal

Crystal structure	monoclinic
Density (g/cm^3)	7.2
Radiation length (cm)	1.14
Nuclear int. length (cm)	20.9
Moliere radius (cm)	2.07
Light yield (ph/MeV)	25000
Light peak emission (nm)	420
Decay time (ns)	40
Refractive index (at λ_{peak})	1.82
Radioactive	Yes
Hygroscopic	no
Radiation hardness (Gy)	> 10^4

Table 3.1 – LYSO features

As it is possible to see from the table above, LYSO shows high density and high light output, its drawback consists in an intrinsic radioactivity due to a contamination of ^{176}Lu isotope.

Figure 3.10 shows the ^{176}Lu nuclide decay scheme. This isotope decays beta minus with a maximum electron energy of 596 keV followed by emission of three prompt gamma photons with energies of 88, 202 and 307 keV, therefore producing a not negligible background comprised in the interval 200-500 KeV.

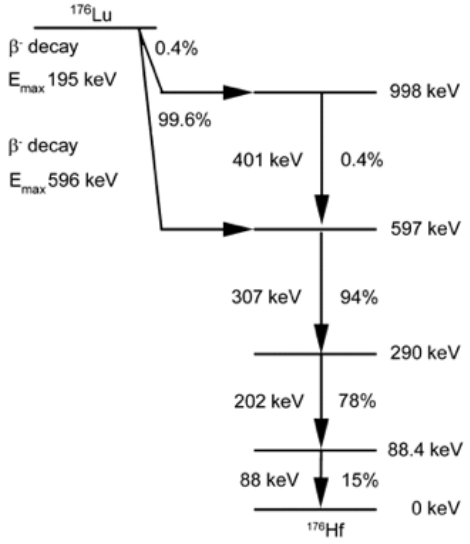

Figure 3.10 - Lutetium decay scheme

Figure 3.11 shows the energy spectrum of LYSO intrinsic radioactivity acquired for 14400 seconds with a C.A.E.N. DT5720B digitizer. In the figure the peak at 300 KeV and the superimposed beta-decay spectrum are visible.

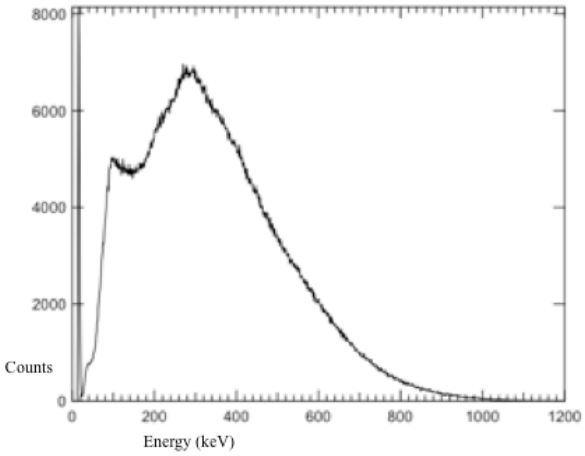

Figure 3.11 - LYSO background spectrum

Originally a PMT readout was chosen to measure the parameters of interest but the intrinsic radioactivity of the sample interfered with the data acquisition system. Finally the choice was made for a measurement in coincidence. In the next section a description of the laboratory experimental set-up used is given.

– Experimental setup description

As stated earlier, the reduction of LYSO background was approached with the coincidence detection method using an additional PMT coupled to a cylindrical Yap-Ce crystal scintillator (3cm diameter, 1mm thickness), a source of coincident photons and a coincidence circuit.

For the acquisition of coincidence events, a ^{22}Na gamma source was choosen.

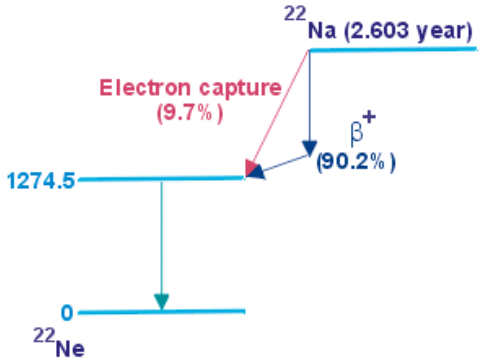

Figure 3.12 - ^{22}Na decay scheme

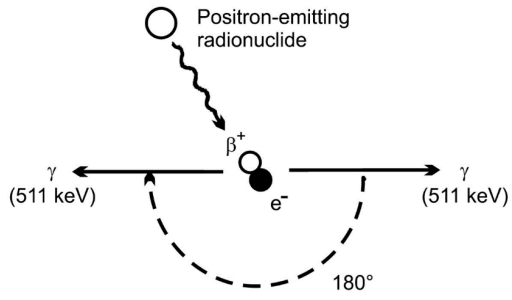

Fig.3.13 - Process of positron emission and subsequent positron-electron annihilation resulting in two 511 keV annihilation photons emitted 180° apart.

As it is possible to see from the decay scheme shown above in figure 3.12, this isotope decays (in 99.95% of cases) via positron emission or electron capture to the first excited state of the ^{22}Ne at 1.274 MeV (with a subsequent emission of a gamma photon). The positrons emitted by the source annihilate in the material that acts as a support to the source, producing two gamma photons each one with energy of 511 keV. These two fotons are emitted back-to-

back and in coincidence with each other and reach the two detectors nearly simultaneously to be successively detected by the coincidence circuit.

The circuit consists of a series of modules arranged in such a way to analyze the pulses from each detector, decide if the pulses are in coincidence and if so to generate a gate and to trigger the data acquisition system. With this procedure all the events that are not simultaneous are suppressed.

Figures 3.14 and 3.15 show a scheme and a picture respectively of the experimental set-up used.

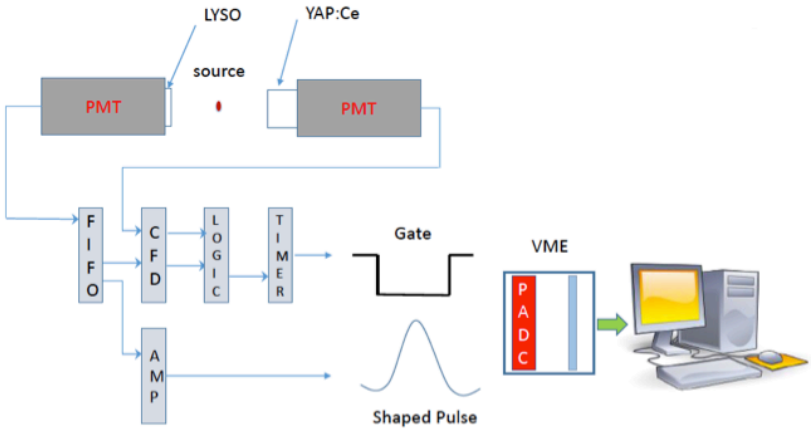

Figure 3.14 – Scheme of the experimental set-up used for coincidence measurements

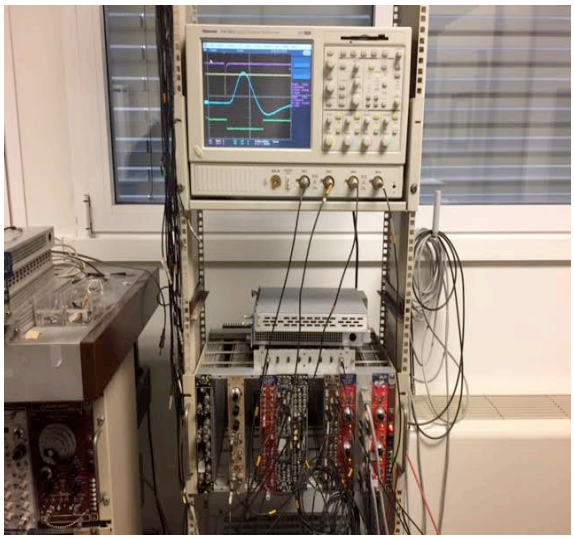

Figur3 3.15 – Picture of the coincidence circuit

The readout of the LYSO scintillator was performed using a Hammamatsu R329-2 photomultiplier tube which quantum efficiency well matched the LYSO light peak emission.
The two scintillators were attached to the photocathode by means of optical grease in order to minimize optical loss between the scintillator and the photocathode and were connected to a high voltage power supply (C.A.E.N. Power Supply, Mod. N471). The positron source was placed in a polystyrene holder and it was positioned centrally between the two PMTs. The signal from the first photomultiplier tube was sent to the input of a Linear Fan-In/Fan-Out device (Phillips Scientific 744). This unit splits the signal providing two separate identical outputs one of which was sent to an amplifier (SILENA Amplifier, mod. 7611/L) having a gain=50. The remaining current output along with the YAP signal anode were connected to a Constant Fraction Discriminator (ORTEC 934). Constant Fraction Discriminator produces two NIM logic pulses using the constant fraction time derivation technique for signal sizes beyond a user selected threshold. CFD was set to its minimum threshold of −30 mV. To account for any relative delays between the two detectors, theese logic pulses were passed through a variable delay unit. The delay was verified using a Tektronix Digital Oscilloscope; a delay of 40 ns in the signal of the second detector was necessary in order to sincronize the two signals. Theese two simultaneous pulses were so connected to a logic coincidence unit (C.A.E.N. Programmable Logic Unit mod. 81A) to generate a gate and to trigger the data acquisition system (DAQ). The GATE width was 500 ns.
A simple modification of the circuit also allowed for the acquisition of data in single mode. In this case the experimental set-up, sketched in figure 3.16, consists only of the LYSO crystal coupled to the Hamamatsu PMT supplied with a voltage of -1200 V, the PMT output is sent to a CAEN DT5720B digitizer.
When in single mode the crystal was irradiated also with ^{241}Am, ^{57}Co and ^{137}CS.

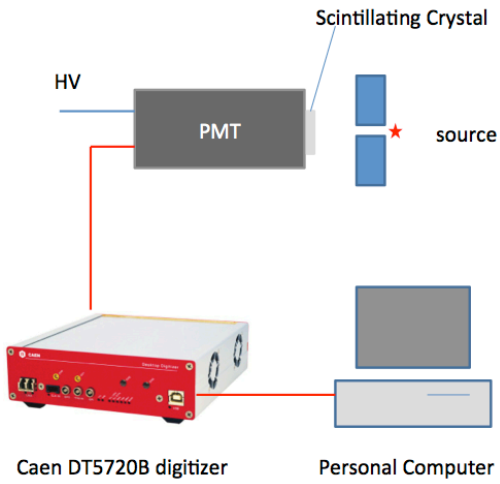

Figure 3.16 - Scheme of the circuit used for the acquisition of data in single mode

Next section shows the spectra acquired with this laboratory equipment and the results obtained.

– Acquired Spectra and results

After the energy calibration of the system, the ^{22}Na coincidence specrtum was acquired. Figures 3.17 and 3.18 show the energy calibration curve and the the coincidence spectrum respectively.

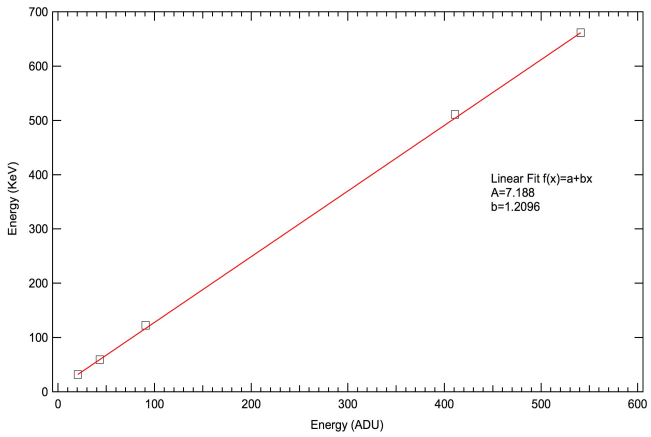

Figure 3.17 - Energy calibration curve. The curve was obtained from the interpolation of four points, one for each source, plus the point correspondig to the X-ray fluorescence peak of Barium at 32.19 KeV.

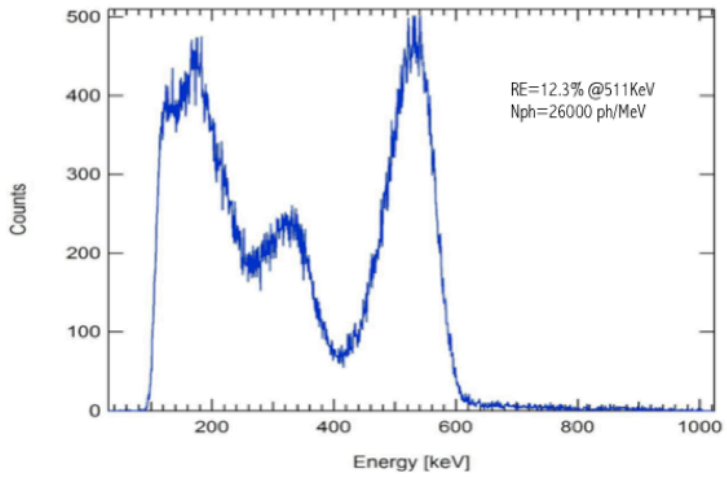

Figure 3.18 – ^{22}Na coincidence spectrum. The peak at 511 KeV corresponding to the ^{22}Na positrons annihilation is clearly seen. The small slope on the left side of the peak is due to fluorescence x rays, while the second smaller peak on the left is the Compton edge.

In the coincidence spectrum shown above, there is a peak at 511 KeV corresponding to the ^{22}Na positrons annihilation. The small slope on the left side of the peak is due to fluorescence x rays, while the second smaller peak on the left is the Compton edge.
The energy resolution of the sample has been evaluated by a gaussian fit performed with the data analisys software *Igor-Pro* and was used to determine the light output of the sample (in unit of *photons per MeV of energy deposition*) according to the equations below:

$$RE = \frac{FWHM}{E} = \frac{2{,}3548}{\sqrt{\alpha \cdot \gamma \cdot n_{ph}}} \cdot \sqrt{\frac{\delta}{\delta - 1}} \tag{3.12}$$

$$n_{ph} = \frac{2{,}3548^2}{\alpha \cdot \gamma \cdot RE} \cdot \frac{\delta}{\delta - 1} \tag{3.13}$$

where n_{ph} is the mean number of incident photons, γ is the quantum efficiency, α is the collection efficiency and $\boldsymbol{\delta}$ is the mean secondary emission yield of each dynode.

An energy resolution at 511 Kev of 12.3% has been obtained and a light yield of about 25 fotons per kev has been evaluated matching the specifications given by the producer.

In figure 3.19 the comparison between the measured and simulated spectrum of LYSO intrinsic radioactivity is shown, figure 3.20 shows the measured spectra of ^{241}Am, ^{57}Co, ^{22}Na and ^{137}Cs acquired in single mode along with those obtained by simulations [36].

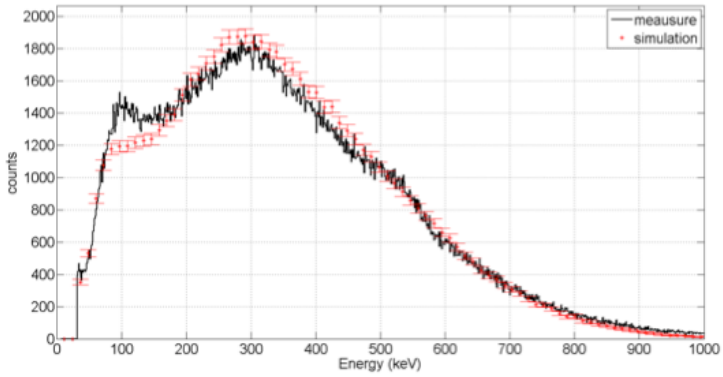

Figure 3.19 – Comparison between measured and simulated spectrum of LYSO intrinsic radioactivity

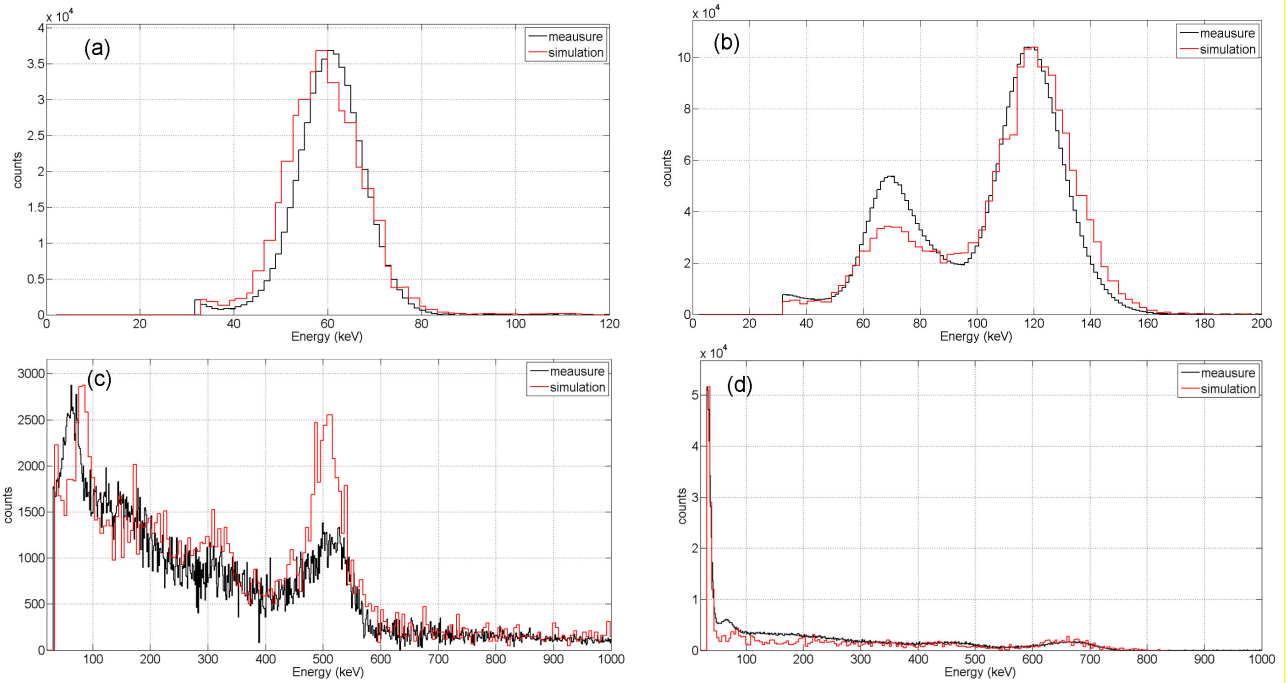

Figure 3.20 - comparison between the measured and simulated spectra of ^{241}Am (a), ^{57}Co (b), ^{22}Na (c) and ^{137}Cs (d).

The simulations were carried out including the generation and tracking of the of optical photons through the measurement set-up,

from the scintillator up to the PMT photocathode where they were converted into photoelectrons.
All the materials relevant for the optical photon transport were included in the simulations, such as an optical grease (EJ-550 Silicone Grease) to match the refractive index of the scintillator with the Glass (BK7) of the PMT, the Bialkali PMT photochatode and a black cardboard positioned in front of the scintillator and used to absorb the photons emitted in the backward direction.
The discrepancy between simulation and experimental results is most likely due to the approximation of the real optical properties of the volumes considered, such as refractive index and absorption length as a function of the optical photon energy and surface roughness. Indeed, in Geant4, the materials have no default optical properties and the relevant parameters have to be provided by the user, who has also to define the scintillation parameters, such as scintillation spectrum, photon yield and decay time constant. An imperfect characterization of the scintillator or of the other materials could explain the difference in the results. A further contribution could be due to an imperfect modelling of the radioactive sources in terms of gamma line emission relative weight.
The results presented are the best approximation obtained by tuning all the simulation parameters simultaneously involved.

In summary, the simulations and the results of this study, useful to characterize LYSO in terms of light yield and intrinsic background, led to choose a 0,5 mm thickness LYSO crystal as target to be mounted on the GPI prototype.

3.2.2 Optycal system configuration

The problem of evaluating the optical system configuration providing the desired performance was approached by the use of the experimental set-up scketched in figure 3.21.

It includes a CCD camera connected to the acquisition system, a lens, a diaphragm and a supporting frame.

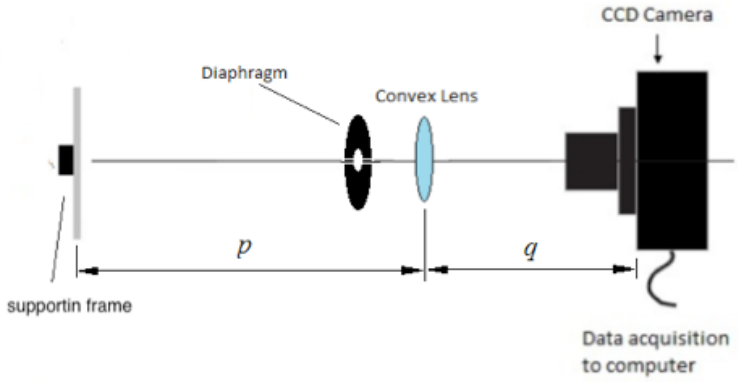

Figure 3.21 - Scheme of the experimental set-up used to test the optical system (lens + CCD camera)

- Camera selection

In the selection process of the CCD camera the following factors were taken into account: low cost, low dark currents, pixel size, sensor size. In particular, the requirements considered for the CCD camera were the following:

- pixel matrix > 512 × 512
- pixel size ~ 10x10μm
- framerate > 1Hz
- pixel bit depth > 12 bit
- dark current < = 1 e-/s
- max acquisition time > 10 s
- Gigabit ethernet communication and control

These specification requirements are quite common and can be satisfied by widely commercially available products by many different manufacturers. Ultimately an astronomcal CCD camera manufactured by SBIG (model ST-8300M) was chosen. Its specifications are reported in the following table.

Sensor size	17.96x13.52 mm
Pixel matrix	3326x2504
Pixel size	5.4x5.4 μm
Binning mode	1x1, 2x2, 3x3
Quantum eff. (420 nm)	36 %
Charge Transfer Eff.	0.999995
A/D Converter	16 bit
A/D Gain	2.7 ADU/e^-
Full Well Capacity	25000 e^-
Read noise	16 e^-
Dark current	1 e^-/s/pixel at 20°

Table 3.2 - Mean features of the SBIG camera, model STT-8300M

- Tested lenses

In order to select a lens system that suits the required magnification and geometrical criteria, different lenses have been considered.

In particular, three Plano-Convex lenses with different focal lenghts (50mm, 75mm and 100mm) and a manual focus *Nikon* lens (85 mm/f1.4) were tested.

- Tests on the Lens-Camera system

In figure 3.22 the assembled experimental setup used to test the lens-camera system is shown.

The whole equipment was assembled in a dark box in order to reduce background illumination and the CCD camera was mounted on a motorized linear stage that allow a linear translation of the camera.

To test the performance of the optical system, a series of measurements was performed in order to evaluate the CCD focus distances, the magnification factor and the depth of field.

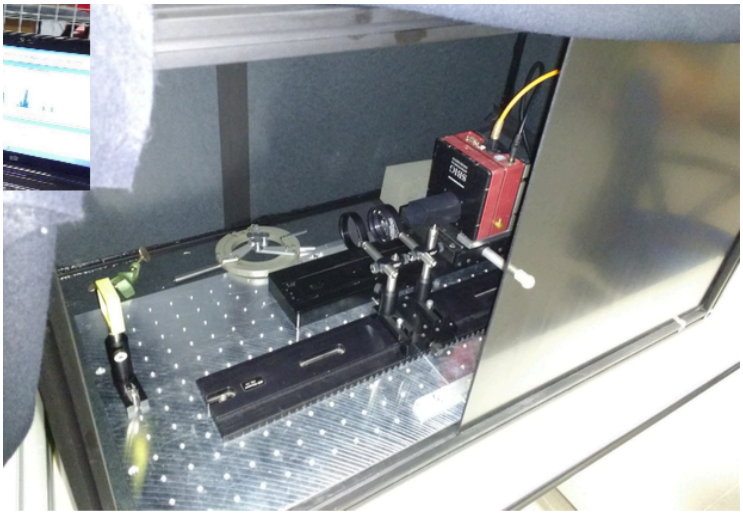

Figure 3.22 – Picture of the experimental set-up used to test the optical system

- Focusing of the optical system

The aim of these measurements was to estimate the focus distance of the CCD camera. As a preliminary test the lens with focal lenght 100 mm was mounted on its support.

The focus distance was first calculated using the thin lens equation, $1/p + 1/q = 1/f$, and then measured with the lens positioned at a fixed distance from the object (370mm) and by moving the position of the camera in a range of distances between 0, relative to the maximum distance between the object and image, and 300 mm.

First acquisitions have been performed without diaphragm and by focusing a test pattern with an exposure time of one second, starting with the camera in the reference position calculated by use of the thin lens equation and moving with a step of one millimeter each acquisition.

Using this configuration no clear sharpness of the images was obtained. This could be due to the lens aperture being too large resulting in an short depth of field. In order to increase the depth of field, a diaphragm was put in front of the lens. In particular, three different diaphragms with diameters of 2mm, 6mm and 17mm were used.

The use of the 2mm diaphragm led to an increase of the exposure time since with an exposure time of only one second the images

were too dark. The proper exposure time was calculated to be 30s; after verifying that longer exposure times could not saturate the CCD camera, a series of acquisitions started with the camera set to 2×2 binning and adapting the exposure time to the different diaphragm apertures.
Image processing, consisting in dark subtraction and contrast adjustment, was performed by use of the Image-J software [37], a specific program deputed to the image processing and depiction.
Figure 3.23 shows two focused images acquired with two different configurations of the system.

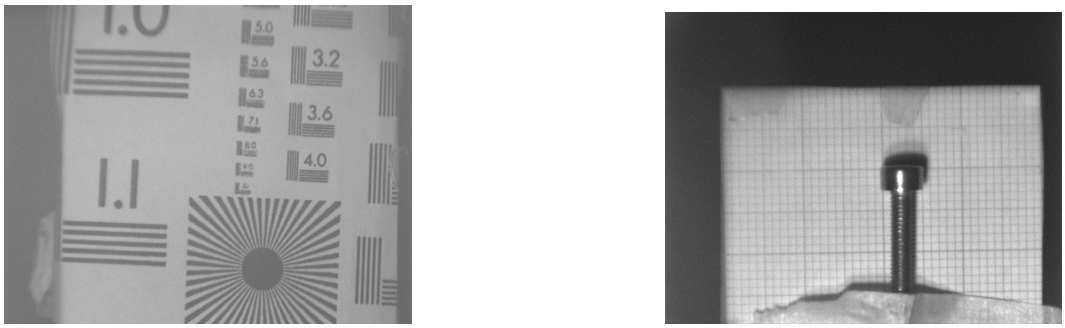

Fig 3.23 – Example of two focused image acquired with two different configurations (Left: f=100mm, D=6mm, t=10s; right: f=100mm, D=17mm, t=1s)

- Evaluation of the magnification ratio

In according to equation 2.26, the magnification of the system was calculated as the ratio of the image showed in figure 3.24 and the actual object size. In particular, we considered the length of five different distances both in the image and in the actual object. As it is possible to see from table 3.3, a magnification factor of about 0.25 was found.

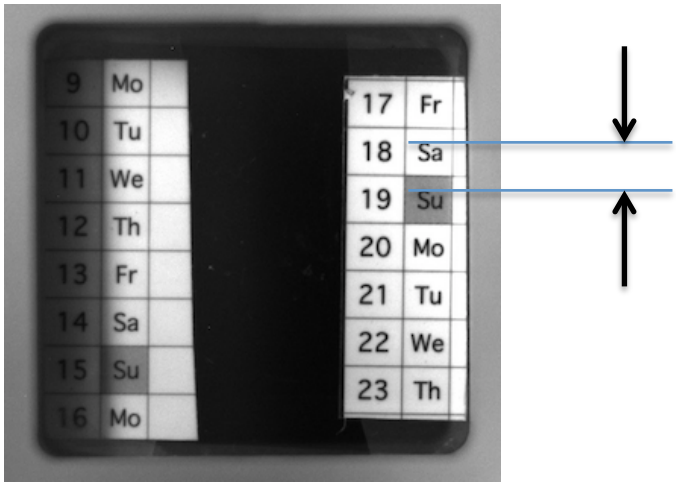

Figure 3.24 – Image used for evaluation of M

Distance	Object size [mm]	Image size [pixels]	M
2 lines	7.3	166	0.245
3 lines	11	253	0.248
4 lines	15	340	0.245
5 lines	18.5	426	0.248

Table 3.3 – Magnification ratio values

- Evaluation of *DoF*

The depth of field is the distance between the nearest and the furthest objects that are in acceptably sharp focus in an image. Since the thickness of LYSO that will be mounted on the GPI is 0,5 mm, a depth of field bigger than 0,5 mm is needed in order to have a complete sharp image of the target and avoid blurring.
The depth of field was calculated for each optical configuration by use of the following equation [35]:

$$DoF = \frac{sf2}{f2 - Ac(s-f)} - \frac{sf2}{f2 + Ac(s-f)} \tag{3.15}$$

where A is the f-number, f is the lens focal lenght, s is the subject distance and c is the circle of confusion. In the image plane c is equal to the dimension of one pixel, that is 10.8μm since we are considering a 2×2 binning configuration.

Tables 3.4 and 3.5 show the values obtained with a 100mm and a 75 mm focal lenght lens and with different diaphragms.

D [mm]	DoF [mm]
2	14.5
6	4.8
17	1.7

Table 3.4 - Values of DoF obtained with lens having f=75 mm and for each diaphram aperture

D [mm]	DoF [mm]
2	10
6	3.3
17	1.2

Table 3.5 - Values of DoF obtained with lens having f=100 mm and for each diaphram aperture

As it is possible to see from the two tables above, these configurations allow to obtain a depth of field greater than 0,5 mm. We can also notice that the DoF decreases with incrising diaphragm diameter and gets bigger for lower focal lenght as aspect.

3.3 - GPI: Final configuration

The results of the tests performed led us to adopt the final prototype configuration sketched in figure 3.25. In this configuration the LYSO is put at a distance of 667 mm from the lens and the resulting magnification is 0.13. The light emitted by the scintillator is focused onto the CCD through the manual focus Nikon 85mm/f1.4 lens. The nikon lens was chosen in order to overcome the limitations of a single lens due to aberrations.

Figure 3.25 – Scheme of the GPI prototype configuration

Figures 3.26 and 3.27 show a 3-D model and a cross-section respectively of the GPI in its final configuration. The system comprises a cross vacuum chamber equipped with a mechanical actuator that allows to drive a target holder in a ultra-high vacuum (10^{-7} mbar) using a bellow. The target holder will allow to position on the gamma beam 3 different targets that can be mounted at the same time, each one having a maximum size of 40 × 40 mm to easily contain the beam spot.

Outside of the vacuum, looking at the target through a quartz viewport, a CCD camera coupled with a proper photographic objective is installed in a dark box to avoid environment light contamination. The viewport is oriented at 45° with respect to the beam direction, allowing to acquire images of the target from a direction perpendicular to the target plan. The camera supporting frame includes a mirror, which reflects downwards the light coming out from the vacuum window.

Also, the camera is mounted on a remotely controlled linear stage for fine focus adjustment. The linear stage allows to move the position of the camera in a range of distances from the target that goes from 586 up to 800 mm. This range of distances permits a safe operation of the CCD. Indeed, the expected dose rate in air at these locations was evaluated through a dedicated Geant4 simulation tool including all the most relevant elements of the collimation and characterization line and resulted to be compatible with the dose rate allowed for radiation protection purposes and therefore suited for electronic devices [32].

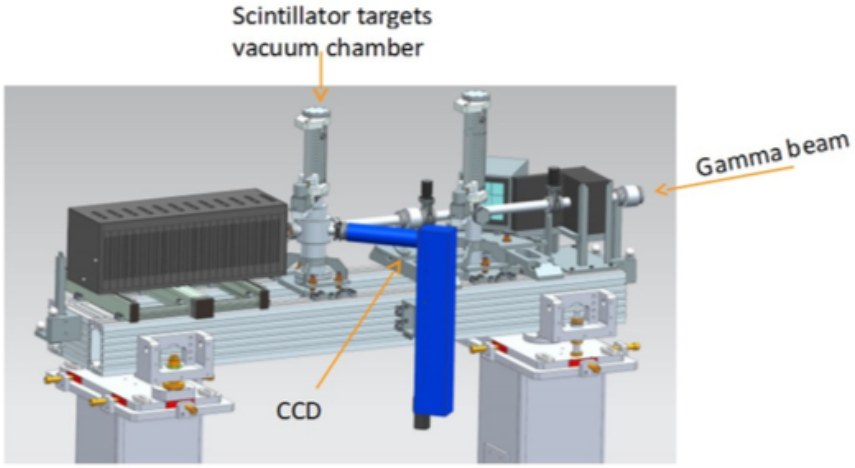

Figure 3.26 - 3D model of the Gamma Profile Imager.
The GPI subsystem is placed on the beamline between the NRSS (upstream) and GCAL (downstream) subsystems

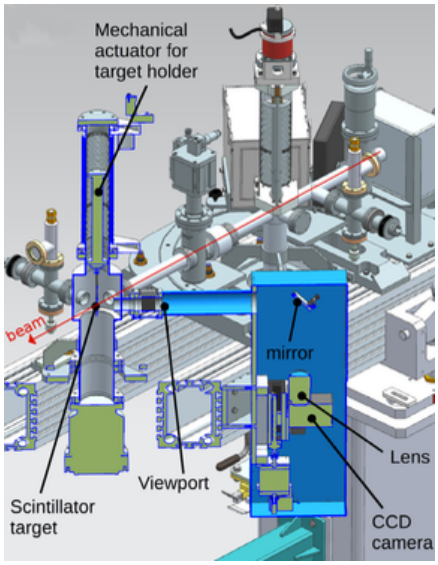

Figure 3.27 – Cross-section of the GPI

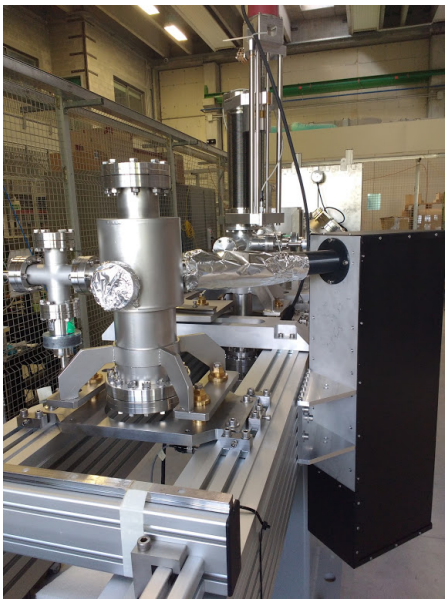

Figure 3.28 - Picture of the assembled system at Ferrara INFN laboratory

Figure 3.28 shows the assembled GPI prototype at INFN Ferrara laboratory . The geometrical configuration is the same of the final design with the exception of the mirror which was not installed due to geometric constraints of the laboratory.

Once the final GPI configuration was selected, a set of experimental tests were performed on the GPI prototype using the photon beam from a Varian M-143T X-ray tube.
In the next chapter the tests performed and the results obtained are described along with the simulations of expected performances with ELI-NP gamma beam.

CHAPTER 4

EXPERIMENTAL TESTS ON GPI PROTOTYPE

A set of experimental tests were performed on the GPI prototype in order to validate the analytical model adopted to evaluate the imaging system response and the signal expected at ELI-NP-GBS.
In this chapter a description of the tests is given in section 4.1. The results of the expected signal evaluated by use of Monte Carlo simulations, performed with Geant4, are reported in section 4.2.

4.1 - X-rays tests on GPI prototype

Tests on the assembled GPI prototype were performed irradiating the system by use of an X-ray tube at LARIX-A laboratory at the University of Ferrara.
The main goal of the tests was to compare the measured signal, in terms of level of grey, with the calculated and simulated data in order to validate the simulation code adopted to predict the response of the system to a realistic ELI-NP gamma beam.
Before carrying out the actual experimental tests, a series of preliminary measurements, described in section 4.1.2, were performed in order to evaluate the magnification factor, the distance of the LYSO from the X-ray tube focus, the exposure and the intrinsic resolution of the imaging system.
In the next section a description of the experimental set-up used to test the GPI prototype is given.

4.1.1 – Experimental setup description

Figures 4.1 and 4.2 show a scheme and a picture respectively of the experimental set-up used; it includes a Varian M-143T X-ray tube, a 0.5 mm LYSO scintillator, a collimator, a filter box, the CCD camera and the Nikon lens both used in the optical measurements described in chapter 3.

Figure 4.1 - Skecth of the experimental setup used to test the GPI prototype

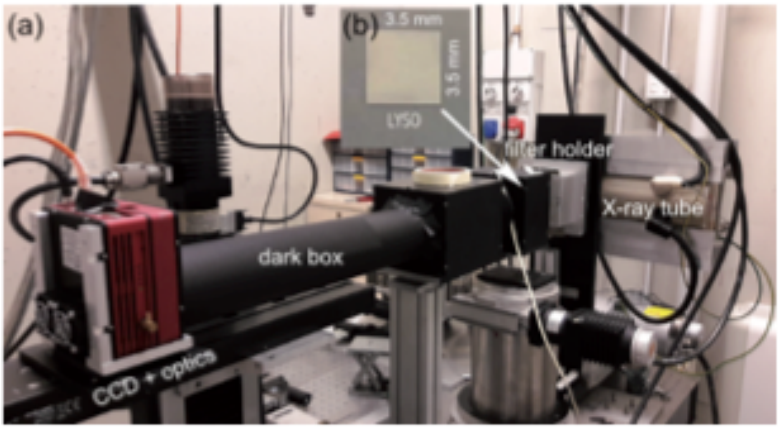

Figure 4.2 - (a) Picture of the experimental setup used to test the GPI prototype. (b) Picture of the scintillator crystal used.

The used X-ray tube features a 0.63 mm Beryllium window and a nominal focal spot size of 0.1 × 0.35 mm^2. The source was powered by a 50 kHz Metaltronica Compact Mammo-HF generator with an adjustable voltage from 20 to 49 kV and was operated in high current mode, which allows short exposition time, 5 seconds maximum, but current higher than 40 mA. The LYSO scintillator was positioned in a dark box securing it with tape at a distance of 667 mm from the Nikon objective lens and 232 mm from the X-ray tube focus. Collimators with hole of various diameter were used to limit the portion of target irradiated by the X-ray beam. The light emitted by the scintillator was focused through the manual focus Nikon 85mm/f1.4 lens onto the SBIG ST-8300M CCD [32].

4.1.2 Preliminary measurements

- Focal spot-lyso distance and magnification factor evaluation

The focal spot-lyso distance was evaluated using the magnificaton formula and the images of an object acquired at two different distances from the crystal. The object was a 9.87mm diameter steel washer set at 5.1mm and 70.62mm from the crystal. The images acquired allowed us to calculate the diameters of the object in pixels and the magnification ratios at the two distances; using this information the focus-crystal distance was determined.

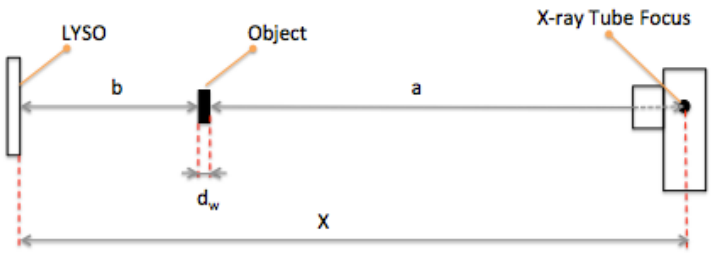

Figure 4.3 – Sketch of the set-up used in the measurement of the focus-crystal distance

With reference to figure 4.3, let a and b be the object-focus and the object-crystal distances respectively, the magnification factor is given by the following equation:

$$M = \frac{(a+b)}{a} \tag{4.1}$$

The size of the object on the LYSO, d_{img}, can be calculated by the formula:

$$d_{img} = \frac{a+b}{a} d_r \tag{4.2}$$

where d_r is the real size of the object.

If X=a+b we can rewrite the formula as follows:

$$d_{img} = \frac{X}{X-b} d_r \tag{4.3}$$

Data relative to the two images for the object set at the distances a and b are reported in the table 4.1:

b [mm]	Diam [pix]
5.1	121
70.62	170

Table 4.1 – values of the washer diameter in pixels at the two distances measured

Using these data along with the equations above a value of 232.4 ± 5.7 mm was found for X and a value of 118.3 ± 1.0 for the actual diameter of the washer in pixels. Being 10.8 um the size of one pixel, a magnification of m=0.1294 was found, corresponding to one pixel in the space-object of 83.4 um.

- Exposure measuremtents

Exposure measurements, performed by use of a ionization chamber, RADCAL mod 10X6-6M, were necessary in order to validate the exposure estimations calculated by SrS [38] and SpekCalc [39], two software that simulate photon spectra from X-ray tubes. Figure 4.4 shows the scheme of the set-up used; measurements have been carried out after the crystal and the light tight box were removed.

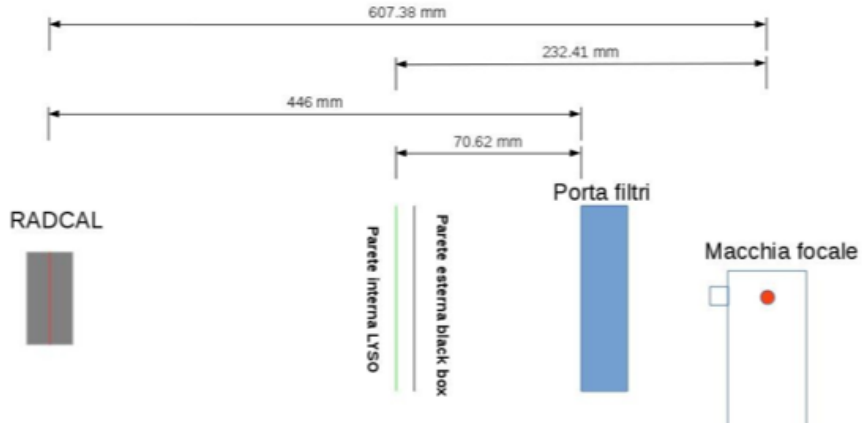

Figure 4.4 – Scheme of the experimental set-up used to perform exposure measurements.

Exposure measurements were performed with a tube voltage ranging from 30 to 40 kVp and various anodic currents. For each configuration five mesaurements have been done and then averaged. The values, obtained in mR/min and showed in the table below, were successively converted in µGy/mAs to make a comparison with data simulated by the softwares.

kVp	mA	Ave [mR/min]	Stdev [mR/min]
30	10	46.00	0.71
30	15	65.60	0.55
30	20	84.40	0.89
30	30	127.46	0.81
35	30	457.40	3.36
40	30	1060.20	4.97

Table 4.2 - Exposure values obtained by use of the ionization chamber

In order to evaluate the linearity of the exposure data in air in function of the current, the values relative to a 30 kVp voltage have been plotted (Figure 4.5).

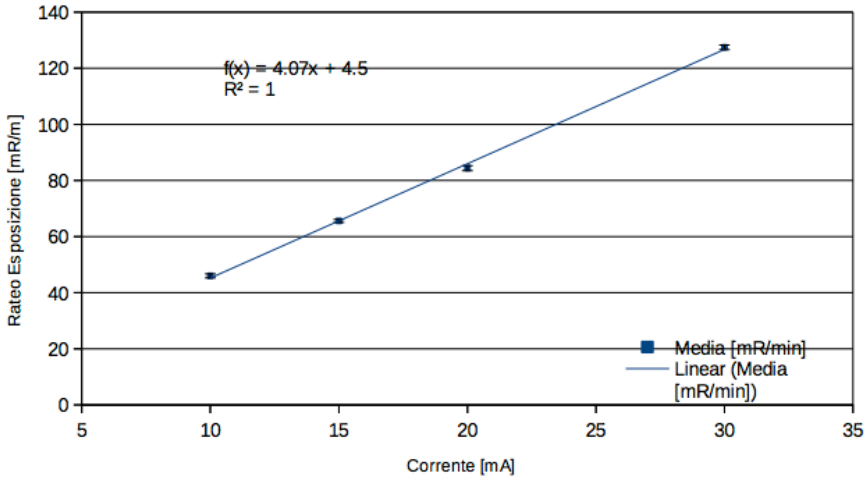

Figura 4.5 – Exposure rate in function of the current

The fit function is a linear function of the type $E = k*(I_n+I_o)$, with $k=4.07\pm0.01$ mR/(mA*m) and $I_0=1.1\pm0.5$ mA. An offset value of

1.15 mA was so found thus it has to be subtracted to the nominal value of the current.
Using the softwares SrS and SpekCalc the fluence of the X-ray beams have been simulated and the calculated values were compared with those determined through measurements. The results in µGy/mAs are reported in table 4.3.

kVp	Radcal[µGy/mAs] at 0.75 m	Stdev [µGy/mAs]	SRS[µGy/mAs] at 0.75 m	SPEKCALC[µGy/mAs] at 0.75 m
30	0.39	0.02	0.42	0.41
35	1.40	0.07	1.59	1.43
40	3.25	0.11	3.78	3.22

Table 4.3 - Comparison of measured and simulated dose rate values.

As we can see from the table above experimental and calculated dose rate values agree, expecially the ones from SpekCalc. In particular, the experimental data are lower by about 12% with respect to the data calculated using SrS. In the case of SpekCalc, measured and calculated data match within the standard deviation.
Considering these differences spectra generate by use of SrS or SpekCalc can be used to analitically evaluate the energy deposited in the LYSO and thus the number of grey levels on ccd.

- **spatial resolution measurements**

The spatial resolution of the imaging system was measured by use of the slit camera method mentioned in chapter 2.
The images of the slit have been acquired by frontally irradiating the LYSO crystal with a X-ray tube voltage of 40 kVp, an anodic current of 30 mA, a CCD exposure time of 2 s, and varying the CCD binning mode (1x1 and 2x2) and the lens f-stop (f/1.4 and f/2).
In the acquired images the background was subtracted and a plugin of the ImageJ software was used to calculate the LSF. Each LSF was fitted using two gaussian distributions.

In the figure 4.6 an image of the slit camera acquired with aperture f/1.4 and exposure time of 2 seconds is shown.

Figure 4.6 - Slit camera image acquired with aperture f/1.4 and exposure time of 2 seconds

In the following table the values obtained with the different configurations are listed.

binning	f/stop	FWHM [μm]	FWTM [μm]	Pixel size[μm]
1	1.4	91.3	406.7	41.5
1	2	83	340.3	41.5
2	1.4	141.1	464.8	83
2	2	128.7	423.3	83

Table 4.4 - FWHM e FWTM values obtained by the LFS acquired with binning 1x1 and 2x2 and f/stop 1.4 and 2.

How it is possible to see from the table above, the intrinsic resolution of the imaging system resulted between 80 μm and 140 μm.

4.1.3 - Testing with x-ray tube

For the acquisition of the signal the X-ray source was set in such a way that the signal obtained was of the same order of magnitude of that expected for the LE line of ELI-NP-GBS [32].
In particular, the scintillator was irradiated for 1 s/shot at 30, 35 and 40 kV using a filtration of 5.1 mm of Al (Alluminum) plus 0.1 mm of Cu (Copper) and increasing the anodic current from 10 to

30 mA. The resulting X-ray spectrum calculated through the SpekCalc software for various voltages is shown in Fig. 4.7.

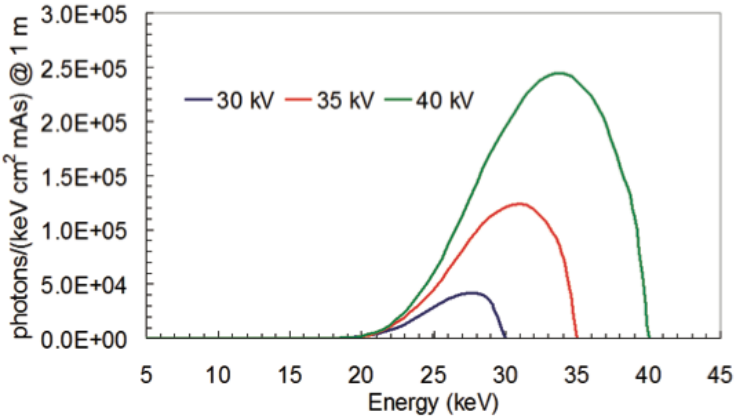

Figure 4.7 - Spectrum of the X-ray tube used to test the GPI pro- totype. The spectrum was calculated through the Spekcalc software for various voltages [32].

Concerning the imaging system parameters, the lens f-stop was set equal to 1.4, the CCD was operated to 2×2 binning mode and its cooling system was fixed at 15 degree Celsius.
The image of the beam spot on the CCD obtained using this configuration is depicted in figure 4.8.

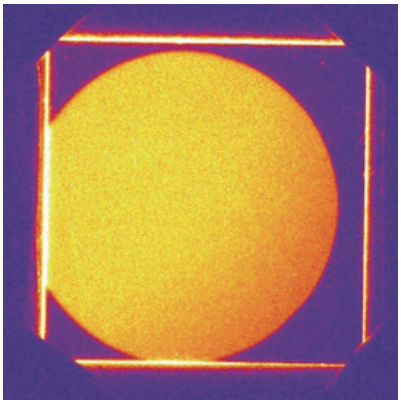

Figure 4.8 - False color image of the spot on CCD. In this case the X-ray beam impinged normally on the scintillator surface passing through a collimator with a hole of 1.23 cm. The light coming out from the edges of the crystal was due to the fact that they have a rounded profile and are not polished [32].

The measured signal, namely the mean value of GL inside the spot on the CCD, was compared to the value estimated using the equation 3.1 with E_{dep}/A calculated through both eq. 3.7 and simulation. The obtained results are summarized in Table 4.5 [36].

V [kV]	I_n [mA]	E_{dep}/A calc [keV/(mm^{2}s)]	E_{dep}/A sim [keV/(mm^{2}s)]	[GL/s] analytical	[GL/s] simulation	[GL/s] Measure
30	10	8.78E+06	9.60E+06	1.40E+2	1.53E+2	1.80E+2±1
30	15	1.37E+07	1.50E+07	2.19E+2	2.39E+2	2.50E+2±1
30	20	1.86E+07	2.04E+07	2.97E+2	3.25E+2	3.20E+2±1
30	30	2.85E+07	3.12E+07	4.54E+2	4.97E+2	4.77E+2±1
35	30	1.42E+08	1.54E+08	2.26E+03	2.45E+03	2.45E+3±1
40	30	4.05E+08	4.50E+08	6.45E+3	7.17E+3	7.37E+3±1

Table 4.5 - comparison between the measured mean value of GL inside the spot on the CCD and the values estimated and simulated

The optics transmission coefficient T and the CCD fill factor FF, namely the parameters which were not exactly known a priori, were reasonably set to 0.8 and 0.95 respectively. Indeed, using these values, the results provided by simulation and measurements, for the case in which the X-ray tube was set to 35 kV and 30 mA, are in perfect agreement. This setting was chosen because the specific energy deposition inside the scintillator is approximately the same of that of the 3 MeV beam of ELI-NP- GBS.
From Table 4.5, it is possible to note a good agreement between measurements and calculations for all settings and that simulations provide a better estimation than analytical calculations.

A further test was carried out by acquiring images with different apertures of the lens diaphragm and binning configurations of the CCD. In particular, two different F-stop values, 1.4 and 2 respectively, and two different binning modes, 1×1 (HR) and 2×2 (MR) respectively, were considered. The results of the measurements are reported in Fig. 4.9 as a function of the specific energy deposition.

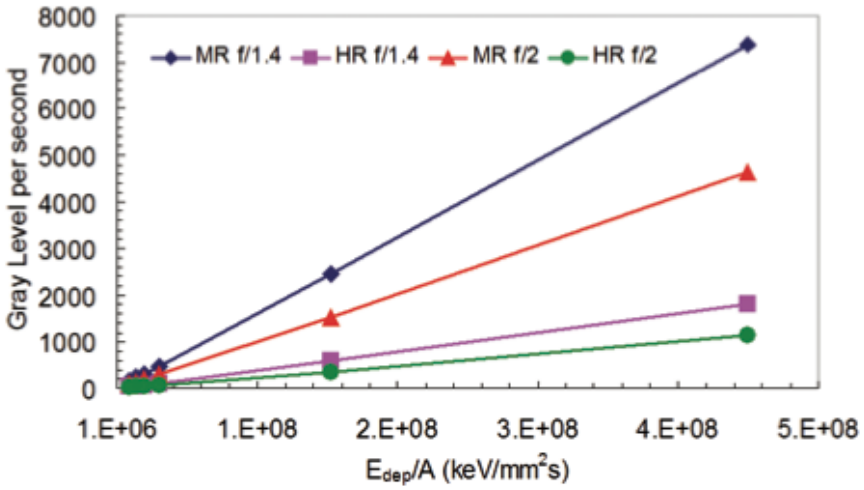

Figure 4.9: Signal measured with various apertures of the lens diaphragm and binning configurations of the CCD [32].

It is possible to note that, the signal scales linearly with the specific deposited energy and that it becomes about 4 times higher when we switch from HR to MR, as expected. A slight discrepancy was found when the lens F-stop if reduced from 2 to 1.4. Indeed, the signal does not double as expected, it gains only a factor 1.6. This discrepancy could be due to a not perfect tuning of the steps of the diaphragm aperture. However, it is possible to take into account this effect in the model introducing a simple correction factor.

A final test was carried out on the GPI prototype to get closer to the real conditions of use. In this case, the X-ray tube was rotated by 45° around the vertical axis and a collimator with a smaller hole was used. The acquired image is shown in Fig. 4.10 and features the expected elliptical shape.

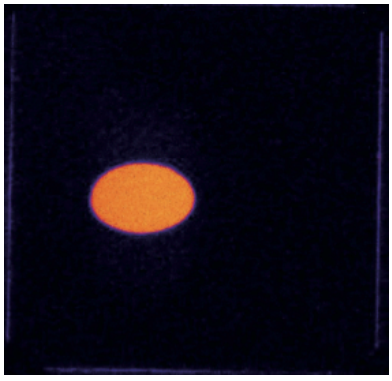

Figure 4.10 - False color image of the spot on CCD. In this case the X-ray beam impinged at 45° on the scintillator surface passing through a collimator with a hole of 2 mm [32].

4.2 Monte Carlo Simulation of ELI-NP-GBS beam

Once the proposed model was validated, the expected signal with the ELI-NP-GBS beam was calculated through simulations. First, the spatial distribution of energy deposition inside a 0.5 mm thick LYSO crystal by collimated gamma beams of various energy was calculated through a set of simulations using Geant4. Then, the signal on the CCD was calculated using the analytical model described in the previous chapter.

Table 4.6 reports the results obtained for various gamma beam energies, setting p = 667 mm, F = 1.4 and 2×2 binning mode [32].

E_{beam} (MeV)	Signal (GL) in 1 s
0.2	3.05E+2
3	2.16E+3
10	2.43E+4
19.5	5.14E+4

Table 4.6 – Expected signal with ELI-NP-GBS beams

The signal ranges from 3.05×10^2 grey level per second at 0,2 MeV to 5.14×10^4 GL/s at 19,5 MeV, therefore, it results to be far above the expected noise of about 45 GL for acquisition time of 1 s and for the overall range of energy.

Moreover, it can be seen that, the lens F-stop and CCD binning configuration can be changed to 2×2 and 1×1 respectively, for the higher energy beams, due to their higher specific energy deposition in LYSO. In this way, the achievable spatial resolution can be increased.

The expected image on the CCD was also simulated. A dedicated paraxial ray-tracing code was developed in matlab language. Starting from the energy deposition distribution calculated before, a number of optical photons were generated randomly inside the scintillator and tracked to the optics and the CCD using the matrix approach. Since the detailed configuration of the Nikon 85mm/f1.4 lens is not known, an equivalent lens, namely a thin

lens with the same aperture diameter and providing the same magnification of the real lens, was considered.

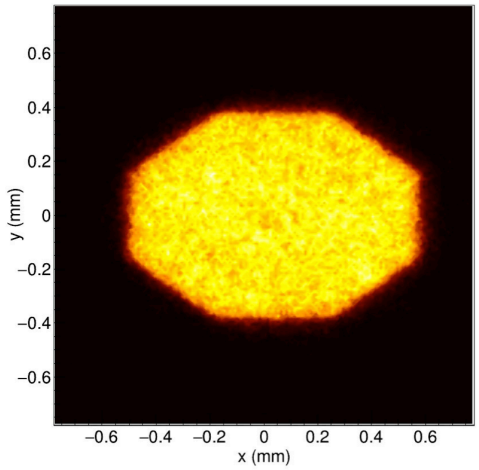

Figure 4.11 - Simulated image of the 3 MeV beam on the CCD [32].

Figure 4.11 shows the simulated image in the case of the 3 MeV gamma beam. It is clearly possible to recognize the expected octagonal shape due to the peculiar collimation system. The image results enlarged along x axis due to the fact that the gamma beam impinges onto the scintillator target at angle of 45°. During the operation phase of the GPI, this stretching effect can be easily corrected in post-processing without the risk of introducing artefacts.

The results obtained by simulations prove that the designed imaging system will allow to acquire significant images of the ELI-NP gamma beams at nominal operations in a small amount of time (~ 1 s) and for the entire energy range of the gamma beam making it possible to check the alignment and the spatial distribution of the gamma beam, both in commissioning and operation phase.

CONCLUSIONS

The activities described in this work concern the design study of the Gamma Profile Imager (GPI) and the following assembly and testing of a GPI prototype.
This device is part of the ELI-NP Gamma Beam Characterization System and is used to measure the spatial distribution and uniformity of the beam and to check the correct alignment of the collimation system with the source of the gamma beam emission.
It consists of a scintillator target intercepting the gamma beam at an angle of 45° and a system, composed of a CCD camera and a related lens, capable of acquiring the light emitted by the target.
The design study started with the selection of the target material and was conducted by performing a characterization test on a sample of 0.5 mm thick LYSO crystal. According to simulations, it has been seen that LYSO gives the best performances in comparison to other inorganic scintillators in terms of efficiency, energy resolution and light yield, therefore it was choosen as target to be mounted on the GPI.
Successively, the performances of the optical system, consisting in lens+CCD camera, were investigated performing a series of measurements aimed to evaluate the CCD focus distances, the magnification factor and the depth of field. Different lenses were considered and tested in order to find the proper configuration capable to suit the required specifications taking into account the geometrical constraints.
Once the whole GPI design was defined, a prototype was assembled and tested by use of an X-ray tube at the I.N.F.N. laboratory of Ferrara.
The main goal of the tests was to validate the analytical model developed to predict the signal expected on the CCD at ELI-NP-GBS as a function of the system configuration.

For the acquisition of the signal onto the ccd, the X-ray tube was set in such way to have a signal of the same order of magnitude of that expected for ELI-NP-GBS.
The cross-check of the experimental CCD signals with the MonteCarlo has provided the tuning of the simulation parameters. By comparison with obtained data, a good agreement was noted between measures and calculations and that simulations provided a better estimation than analytical calculations.
Once the proposed model was validated, the expected signal with the ELI-NP-GBS beam was calculated trough simulations for various gamma beam energies. The signal resulted to be far above the expected noise of about 45 GL for acquisition time of 1 s and for the overall range of energy of ELI-NP.

In summary, this work contributed to the final design of GPI and allowed to validate the simulation code adopted to evaluate, using the realistic parameters, the expected performances on ELI-NP beam.
The results obtained by simulations, in fact, proved that the designed imaging system will allow to acquire significant images of the ELI-NP gamma beams at nominal operations in a small amount of time (~ 1 s) and for the entire energy range of the gamma beam making it possible to check the alignment and the spatial distribution of the gamma beam, both in commissioning and operational phase.

Further planned activities include the testing of GPI prototype in vacuum chamber, the installation and testing of the entire collimation and characterization system at Ferrara I.N.F.N. laboratories and the shipment and installation of each system at ELI-NP site.
At the present these activities are standing by as the proceeding of the project has come to a stop because of contractual issues.

BIBLIOGRAPHY

[1] Extreme Light Infrastructure (ELI). http://www.eli-laser.eu/index.php, Ottobre 2015.

[2] European Project Extreme Light Infrastructure ELI. http://www.extreme-light-infrastructure.eu/.

[3] European high-level experts from alla field of reaserch. European roadmap for research infrastructures, report 2006. https://ec.europa.eu/research/infrastructures/pdf/esfri/esfri_roadmap/roadmap_2006/esfri_roadmap_2006_en.pdf, 2006.

[4] Extreme Light Infrastructure Nuclear Physics ELI-NP. http://www.eli-np.ro/.

[5] The ELI-Nuclear Physics working groups. The white book of eli nuclear physics. www.eli-np.ro/documents/ELI-NP-WhiteBook.pdf, 2010.

[6] O. Adriani et al., "Technical design report eurogammas proposal for the eli-np gamma beam system," *arXiv:1407.3669*, 2014. https://www.researchgate.net/publication/263930417_Technical_Design_Report_EuroGammaS_proposal_for_the_ELI-NP_Gamma_beam_System.

[7] Horia Hulubei National Institute of Physics and Nuclear Engineering - IFIN HH. Bucharest - Magurele. http://www.nipne.ro/.

[8] EuroGammas Association. http://www.e-gammas.com/, 2014.

[9] W. Brown and F. Hartemann. "Three-dimensional time and frequency- domain theory of femtosecond x-ray pulse generation through thomson scattering". *Physical Review Special Topics Accelerators and Beams, 7(6):1–20, 2004.*

[10] V. Petrillo, a. Bacci, R. Ben Alì Zinati, I. Chaikovska, C. Curatolo, M. Ferrario, C. Maroli, C. Ronsivalle, a.R. Rossi, L. Serafini, P. Tomassini, C. Vaccarezza, and a. Variola. "Photon flux and spectrum of Compton sources". *Nuclear Instruments and Methods in Physics Research Section A: Accelerators, Spectrometers, Detectors and Associated Equipment,* 693:109–116, nov 2012.

[11] E. Esarey, S.K. Ride, and P. Sprangle. "Nonlinear thomson scattering of intense laser pulses from beams and plasmas". *Physical Review E,* 48(4), 1993.

[12] L. Serafini et al. "Technical design report of the e-gammas proposal for the eli-np gamma beam system", 2013.

[13] C. Curatolo. *High brilliance photon pulses interacting with relativistic electron and proton beams*. Phd Thesys, Università di Milano, 2016.

[14] G. Paternò, P. Cardarelli, M. Marziani, E. Bagli, F. Evangelisti, M. Andreotti, M. Gambaccini, V. Petrillo, I. Drebot, Bacci, C. Vaccarezza, A. Variola, and L. Palumbo. "A collimation system for eli-np gamma beam system design and simulation of performance". *Nuclear Inst. and Methods in Physics Research, B*, pages 1–5, 2016.

[15] P. Cardarelli, G. Paternò, G. Di Domenico, E. Consoli, M. Marziani, M. Andreotti, F. Evangelisti, S. Squerzanti, M. Gambaccini, S. Albergo, G. Cappello, A. Tricomi, B. Zerbo, M. Veltri, O. Adriani, R. Borgheresi, G. Graziani, G. Passaleva, A. Serban, O. Starodubtsev and A. Variola. "Gamma beam collimation and characterization system for ELI-NP-GBS". *Proceedings of the European Nuclear Physycs Conference, 21018.*

[16] R. Borgheresi, O. Adriani, S. Albergo, M. Andreotti, G. Cappello, P. Cardarelli, R. Ciaranfi, E. M. G. Consoli, G. Di Domenico, F. Evangelisti, M. Gambaccini, G. Graziani, M. Lenzi, F. Maletta, M. Marziani, G. Passaleva,G. Paternò, A. Serban, S. Squerzanti, O. Starodubtsev, A. Tricomi, M. Turisini, A. Variola, M. Veltri and Bruno Zerbo. "A Characterization System for the Monitoring of ELI-NP Gamma Beam". Proceedings of The 7th International Conference on New Frontiers in Physics, 2019, 13, 9.

[17] M.Gambaccini et al., D081- "gamma beam characterization design report", 03 2015.

[18] http://www.radiation-therapy-review.com/Photon_Interaction.html.

[19] Interaction of gamma-rays with matter. http://www.fe.infn/radioactivity/educational/detection.html.

[20] P. Cardarelli. *Devices and techniques for the characterization of inverse Compton sources"*. Phd Thesys, Università degli Studi di Ferrara, 2013.

[21] S.G. Anderson, C.P.J. Barty, S.M. Betts, W.J. Brown, J.K. Crane, R R Cross, D.N. Fittinghoff, D.J. Gibson, F.V. Hartemann, J. Kuba, G.P. LeSage, J.B. Rosenzweig, D.R. Slaughter, P.T. Springer, and a.M. Tremaine. "Short-pulse, high-brightness X-ray production with the PLEIADES Thomson-scattering source". *Applied Physics B: Lasers and Optics,* 78(7-8):891–894, May 2004.

[22] W. R. Leo. *Techniques for Nuclear and Particle Physics Experiments*. Springer-Verlag, 1994.

[23] https://www.crystals.saintgobain.com/sites/imdf.crystals.com/files/documents/product-comparisons-inorganic-organic-gas-flowporportional- counters_70286.pdf.

[24] A Guide to CCD Camera Parameters. https://offers.the-scientist.com/hubfs/downloads/TS/ProteinSimple/Imaging/Guide_to_CCD_Camera_Parameters.pdf .

[25] M. Bononi. *Development of a Gamma Profile Imager (GPI) for the beam monitoring of ELI-NP*. Master's degree Thesis, Universitá degli Studi di Ferrara, 2015-2016.

[26] https://en.wikipedia.org/wiki/Spectral_sensitivity.

[27] hammamatsu.magnet.fsu.edu/article/ccdsnr.html.

[28] http://farside.ph.utexas.edu/teaching/302l/lectures/node140.html.

[29] Resolution of iccd cameras. https://stanfordcomputeroptics.com/download/resolution_iccd_mtf.pdf .

[30] X-Ray-Based Medical Imaging and Resolution. https://www.ajronline.org/doi/pdf/10.2214/AJR.14.13126.

[31] EuroGammaS, WP09 status - Gamma beam collimation and characterisation, ferrara, 12 luglio 2017.

[32] P. Cardarelli et al. "A gamma beam profile imager for eli-np gamma beam system". *Nucl. Instr. and Meth. in Phys. Res. A*, vol. 893, pp. 109 – 116, 2018.

[33] Jianming Chen, Liyuan Zhang, and Ren yuan Zhu. "Large size lso and lyso crystal scintillators for future high-energy physics and nuclear physics experiments". *Nuclear Instruments and Methods in Physics Research Section A: Accelerators, Spectrometers, Detectors and Associated Equipment*, 572(1):218 – 224, 2007. Frontier Detectors for Frontier Physics.

[34] R. Mao, L. Zhang, and R. Y. Zhu. "Optical and scintillation properties of inorganic scintillators in high energy physics". *IEEE Transactions on Nuclear Science*, 55(4):2425 – 2431, Aug 2008.

[35] Ren-Yuan Zhu. *The next generation of crystal detectors*. volume 9593, pages 9593–9593, 2015.

[36] G. Paternò, P. Cardarelli, G. Di Domenico, E. Consoli and M. Gambaccini. "Design and simulation of a Profile Imager for the ELI-NP Gamma Beam System". 103° Congresso Nazionale della Società Italiana di Fisica, Trento, 11-15 settembre 2017.

[37] https://imagej.nih.gov/ij/download.html.

[38] Catalogue of Diagnostic X-ray Spectra and Other Data" IPSM Report No 78, (IPSM PO Box 303 York) (1978).

[39] https://iopscience.iop.org/article/10.1088/0031-9155/54/19/N01.